JOURNAL OF GEOPHYSICAL RESEARCH, VOL. 98, NO. B3, PAGES 4231–4259, MARCH 10, 1993

Numerical Simulation of Collapsing Volcanic Columns

FLAVIO DOBRAN[1] AND AUGUSTO NERI

Gruppo Nazionale per la Vulcanologia, Università di Pisa, Pisa, and Istituto Nazionale di Geofisica, Rome, Italy

GIOVANNI MACEDONIO

Consiglio Nazionale delle Ricerche, Centro di Studio per la Geologia Strutturale e Dinamica dell'Appennino, Pisa, Italy

A complex thermo-fluid dynamic model was employed to model collapsing volcanic columns. The two-phase flow model accounts for the mechanical and thermal nonequilibrium between the gas and solid particles. The gas phase involves water vapor and air, and the solids phase involves only one particle size class. The particle collisions, which produce particle viscosity and pressure, were modeled by a kinetic theory model in terms of the granular temperature, whereas the gas phase turbulence was modeled by a turbulent subgrid scale model. The partial differential equations of conservation of mass, linear momentum, energy, and granular temperature were numerically solved for an axisymmetric flow configuration with different vent diameters and two-phase flow conditions. The numerical solutions involved different grid sizes and computational domains in order to assess the adequacy of the model and computational procedure. The results from simulations of collapsing volcanic columns show how after an initial period of fountain building the columns collapse and build radially spreading pyroclastic flows and inward moving column material which is recycled by the columns. For a low-height collapsing column it was found that the fountain reaches a steady state height, whereas for columns with collapsing heights of several kilometers and fine computational grids the fountain heights vary cyclically with periods which are influenced by the dynamics of material recirculation into the columns. The radially spreading pyroclastic flows of the collapsed columns were found to develop convective instabilities whereby rising clouds of gas and particles are developed on the top of the flows. In very large scale volcanic eruptions the numerical results predicted multiple rising clouds on very thick pyroclastic flows. The results from simulations were shown to be consistent with simple column modeling approaches, laboratory experiments, and field observations.

INTRODUCTION

Explosive volcanic eruptions release gas and pyroclastic material into the atmosphere. The released gas is produced from the exsolution of the dissolved gas in magma or from the steam produced by an interaction of magma with aquifers. The violence of a volcanic eruption can be associated with the overpressure of the volcanic jet at the vent and with its effusive energy which in turn are related to the characteristics of magma and volcanic system beneath the surface of the Earth and on the nature of the planetary atmosphere [*Wilson and Walker*, 1987; *Dobran et al.*, 1990]. The important processes associated with the pyroclastic-atmospheric interaction include jet thrusting near the vent, convective mixing of gases and pyroclasts with the atmosphere, and pyroclastic flows.

The near-surface geometry of a volcano can have a pronounced influence on the structure of a jet [*Kieffer and Sturtevant*, 1984; *Kieffer*, 1984]. Large gas-pyroclasts pressures at the vent more easily fracture near-surface rocks and form large craters, modifying in the process the nature of multiphase flow above the vent. The unconsolidated nature of near-surface rocks permits an easy formation of craters or erosion of conduit wall by the escaping gas-pyroclasts mixture, and large jet overpressures cannot be created at the vent. The plinian eruption columns form near pressure-balanced jets because they commonly emerge through craters and enter the atmosphere near or at the atmospheric pressure and produce typical crater lengths of no more than several hundred meters [*Kieffer*, 1984]. The speed of sound of a mixture of gas and particles (pyroclasts) can be very low, and the volcanic jets normally exit into the atmosphere in supersonic flow, producing complex flow patterns above the vent in the form of shocks or compression and rarefaction waves. Since the mean density of gases and pyroclasts in the jet thrust region is normally larger than the density of the undisturbed atmosphere in the vicinity of the jet, the volcanic ejecta penetrate into the atmosphere because of the high momentum of the jet. This high-momentum jet is also a high-temperature jet that heats the air, and upon mixing with it the mean density of the mixture can be reduced below the atmospheric density at the same height. When this occurs and the thrusting momentum of the jet is reduced to near zero, the buoyancy force allows the mixture of gases and small particles (typically less than several tens of microns) to ascend further like a hot plume. If enough air cannot be entrained with the thrusting volcanic ejecta to create a positively buoyant jet, the gas-particle mixture collapses back to the Earth's surface and forms pyroclastic flows and surges [*Sparks and Wilson*, 1976].

Pyroclastic flows involve dense, ground-hugging, high-velocity clouds of gas and entrained particles that may form from laterally directed explosive eruptions or from the collapse of convectively unstable eruption clouds [*Sparks and Wilson*, 1976; *Wright et al.*, 1980; *Walker*, 1985; *Wilson and Walker*, 1987]. *Sparks and Wilson* [1976] note that magmas with high water contents (above about 5 wt %) exiting from conduits are likely to form convective motions,

[1]Also at Applied Science Department, New York University, New York.

Paper number 92JB02409.
0148-0227/93/92JB-02409$05.00

whereas magmas with low water contents or high proportions of CO_2 will form columns with mean densities greater than the atmosphere and thus produce gravitational column collapse and generate ignimbrite-forming pyroclastic flows.

The material in an eruption column is a multiphase and multicomponent mixture that may consist of several gases (water vapor, CO_2, air, etc.) and of a dispersion of liquid (water drops and liquid magma) and solid particles (pyroclasts). The plinian eruption columns exhibit particle sizes from few microns to several centimeters, with about 90 wt % of solids exhibiting a particle size less than 5 cm and 40 wt % less than 600 μm [*Sparks and Wilson*, 1976]. *Walker* [1981] also notes that in ultraplinian and most powerful plinian events 85% of the total ejecta are of submillimeter size and that 60% can be fine ash (less than 63 μm). The plinian and ultraplinian eruptions thus produce a quantity of fine ash which depends on the magnitude (total volume or mass of material erupted) of the eruption and on its dissipative power (areal extent of dispersal). The ignimbrite eruptions form fountains and produce columns from pyroclastic flows. The ignimbrites appear to consist predominantly of submillimeter particles with a fine ash content from 15 to 85 wt % [*Walker*, 1981]. The co-ignimbrite clouds, or the volcanic clouds formed from ignimbrites, contain fine ash which comes partly from the eruption and fragmentation of pumice as the particles collide with one another in the pyroclastic flow or with other objects, and partly from the posteruptive expansion and bursting of gas bubbles in the pumice. The phreatomagmatic eruptions have even larger contents of fine ash than plinian or ultraplinian eruptions. In contrast, the strombolian eruptions tend to be poorly fragmented, with particle sizes which are larger than 1 mm constituting about 95 wt % [*Self et al.*, 1974; *Walker*, 1973]. The larger the particle size of pyroclastic material the larger will be the mechanical and thermal disequilibrium or velocity and temperature differences between the gas and particles in the jet thrust region, convective region, and pyroclastic flow.

The recent laboratory experiments of *Carey et al.* [1988] performed with jets of fresh water and solid particles penetrating into a saltwater solution may be used to infer the nature of different types of volcanic columns. At low particle concentrations the two-phase flow plumes behave similarly as single-phase plumes with the effect of particles being to reduce the buoyancy force. At higher particle concentrations the two-phase flow plumes exhibit several different behaviors. When a plume is dilute, the gravity flows begin to spawn off the side of the plume margins because the margins are denser than the surroundings and the plume interior. At high particle concentrations, however, plumes develop fountains and collapse asymmetrically to generate gravity currents. When the particles in the gravity flows begin to settle, the resulting low-density current becomes buoyant and transforms into a rising plume. This rising plume then merges into the fountain to form a buoyant cloud. The noncollapsing plume may be associated with a plinian eruption column, whereas the collapsing plume, which produces an unstable gravity current, may be associated with a co-ignimbrite cloud rising from the pyroclastic flow [*Carey et al.*, 1988; *Wilson*, 1976; *Bursik and Woods*, 1991].

The volcanic column models based on the steady state and single-phase flow plume theory [*Woods*, 1988; *Bursik and Woods*, 1991] have proved adequate in modeling some of the global characteristics of the plinian and co-ignimbrite columns when the pressure of the gas-pyroclasts mixture at the vent is equal to the atmospheric pressure and the particle concentration in the plume is very dilute. These plume models cannot, however, model dense flows in the fountains and pyroclastic flows and cannot be used to study the complex thermo-fluid dynamic processes that may be associated with real volcanic columns. For this purpose, a more complex transient, multidimensional, and multiphase flow modeling is required.

Workers at Los Alamos National Laboratory [*Wohletz et al.*, 1984; *Valentine and Wohletz*, 1989*a*, *b*; *Wohletz and Valentine*, 1990; *Valentine et al.*, 1991, 1992] carried out the most complex transient, two-phase flow, and two-dimensional simulations of volcanic columns to date by numerically solving the heat, mass, and momentum transport equations of gas and pyroclasts. These simulations demonstrate that nonlinearities inherent in multiphase fluid dynamics, heat, and mass transfer can produce complex phenomena in the column. The most important results from these simulations include the transient behavior of gas-pyroclasts mixture above the vent even after several minutes of the steady state flow discharge from the vent. For conditions typical of fountain-forming silicic eruptions, the unsteadiness in temperature, plume density, velocity, and particle concentration can be associated with recirculation of pyroclastic flow material into the base of the column, ash entrainment from the top of the pyroclastic flow by atmospheric inflow back towards the column, and waves reflecting within the pyroclastic flow if it encounters topographic obstacles. It is thus dangerous to associate the compositional gradients within a magma chamber with compositional gaps in the outflow units or pyroclastic deposits, because the compositional gaps may occur entirely due to interaction of eruption and emplacement dynamics with topography.

The complex two-phase flow modeling of *Wohletz and Valentine* [1990, 1991] and *Wohletz et al.* [1984] sets the stage for complex modeling of volcanic columns in the future. In this model it is assumed that the erupting gas and air have the same chemical composition and that the gases obey the ideal gas equation of state. In real terrestrial eruptions, however, the most significant erupting gas is usually water vapor, and upon coming in contact with atmosphere it may create unstable density stratifications and condense. Some further limitations of the above modeling approach are that the model ignores the solids pressure and viscosity created by the particle collisions, ignores modulation of gas turbulence by the pyroclasts, and involves a crude gas turbulence modeling assumption and a single particle size class. In fountain- and pyroclastic flow-forming volcanic columns the particle collisions and buoyancy effects are expected to be very important, and a modeling approach should adequately account for these physical processes. The past numerical modeling of volcanic columns also lack considerations of the numerical accuracy of results. This is a serious omission of past works and should be remedied in the future publications by performing adequate convergence studies of the simulated eruption columns.

The purpose of this paper is twofold: (1) to present a more complete model of volcanic columns than used in the past and (2) to study several collapsing columns in order to assess the validity of the physical model and adopted computational approach in the modeling of complex thermo-fluid dynamic processes. Without such an assessment it is dangerous to use

the model for the studies of real eruptions and infer the compositional gaps in the deposits with the fluid dynamic processes in the column or in the magma chamber. The adopted model involves the transient, two-phase (gas and pyroclasts) and two-component (water vapor and air) flow and accounts for the particle-particle interactions that produce solids pressure and viscosity. This granular flow model also accounts in a more complete manner for the interphase heat and momentum transfer and for gas turbulence by a turbulent subgrid scale model. Using this model, several different columns were simulated which form fountains, pyroclastic flows, and co-ignimbrite-type clouds. These columns form fountains from few hundred meters to several kilometers above the vents, radially spreading pyroclastic flows, sedimentation of particles in the flows, pyroclastic flow instabilities leading to the formation of particle-laden clouds, and merging of clouds into large volcanic plumes. In the process of these studies we also investigated the effects of the computational mesh and domain sizes on the fountain heights and thicknesses and distances reached by the pyroclastic flow heads. The results from these simulations reproduce the laboratory and field characteristics of collapsing columns, reveal rich physics of the fountains and pyroclastic flows, and point to the careful considerations which must be given to the results from numerical computations. The presented axisymmetric studies of volcanic columns required large computational resources and have identified a need for better and more effective modeling of volcanic columns in the future.

DESCRIPTION OF THE MODEL AND NUMERICAL SOLUTION PROCEDURE

The thermo-fluid dynamic two-phase and two-component granular flow model described in this section was adopted from the works of *Ishii* [1975] and *Dobran* [1984, 1985, 1991], who discuss the multiphase flow formulations, and from *Chapman and Cowling* [1970], *Jenkins and Savage* [1983], *Lun et al.* [1984], and *Savage* [1988], who developed kinetic theories of gases and extensions to two-phase flows to describe the effects of the particle-particle interactions.

Mass, Momentum, and Energy Transport Equations of Two-Phase Flow

The mass balance equations of gas and pyroclasts express the conservation of mass of a mixture of gases and solid particles, and of each gas species present in the gas phase. By assuming that water vapor and air are the only gas components present and that no chemical interaction can take place, we have

$$\frac{\partial}{\partial t}\varepsilon_g\rho_g + \nabla\cdot(\varepsilon_g\rho_g\mathbf{v}_g) = 0 \tag{1}$$

$$\frac{\partial}{\partial t}\varepsilon_s\rho_s + \nabla\cdot(\varepsilon_s\rho_s\mathbf{v}_s) = 0 \tag{2}$$

$$\frac{\partial}{\partial t}\varepsilon_g\rho_g y_a + \nabla\cdot(\varepsilon_g\rho_g y_a\mathbf{v}_g) = 0 \tag{3}$$

$$\frac{\partial}{\partial t}\varepsilon_g\rho_g y_w + \nabla\cdot(\varepsilon_g\rho_g y_w\mathbf{v}_g) = 0 \tag{4}$$

where ε is the volumetric fraction of the gas or solids phase, ρ is the mass density, $\mathbf{v}$ is the velocity, y is the mass fraction of gas components, t is the time, and the subscripts g, s, a, and w pertain to the gas phase, solids or pyroclasts phase, air, and water vapor, respectively. The assumption of no chemical reactions taking place between water vapor and air is consistent with the standard atmosphere assumption used in modeling as further discussed below.

The momentum balance equations for gas and solids can be written as

$$\frac{\partial}{\partial t}\varepsilon_g\rho_g\mathbf{v}_g + \nabla\cdot(\varepsilon_g\rho_g\mathbf{v}_g\mathbf{v}_g) = -\varepsilon_g\nabla P_g + \nabla\mathbf{T}_g + \varepsilon_g\rho_g\mathbf{g} + D(\mathbf{v}_s - \mathbf{v}_g) \tag{5}$$

$$\frac{\partial}{\partial t}\varepsilon_s\rho_s\mathbf{v}_s + \nabla\cdot(\varepsilon_s\rho_s\mathbf{v}_s\mathbf{v}_s) = -\varepsilon_s\nabla P_g + \nabla\mathbf{T}_s + \varepsilon_s\rho_s\mathbf{g} - D(\mathbf{v}_s - \mathbf{v}_g) \tag{6}$$

where P_g is the gas pressure, $\mathbf{g}$ is the gravitational body force per unit mass, $\mathbf{T}$ is the stress tensor, and D is the interfacial drag between the phases. $\mathbf{T}$ and D are given below by the constitutive equations.

The energy balance equations for gas and pyroclasts can be written in terms of enthalpy as

$$\frac{\partial}{\partial t}\varepsilon_g\rho_g h_g + \nabla\cdot(\varepsilon_g\rho_g h_g\mathbf{v}_g) = \varepsilon_g\left(\frac{\partial P_g}{\partial t} + \mathbf{v}_g\cdot\nabla P_g\right) + \nabla\cdot(k_g\varepsilon_g\nabla T_g) + Q(T_s - T_g) \tag{7}$$

$$\frac{\partial}{\partial t}\varepsilon_s\rho_s h_s + \nabla\cdot(\varepsilon_s\rho_s h_s\mathbf{v}_s) = \nabla\cdot(k_s\varepsilon_s\nabla T_s) - Q(T_s - T_g) \tag{8}$$

where h is the enthalpy, k is the thermal conductivity, T is the temperature, and Q is the volumetric heat transfer coefficient for the exchange of heat between the gas and pyroclasts. The viscous dissipation effects due to viscosity and drag between the phases are ignored since they are of minor importance in comparison with convection, conduction, and energy exchange between the phases [*Dobran*, 1988].

Constitutive Equations

The modeling equations (1)–(8) can be closed by specifying the constitutive equations for the stress tensor $\mathbf{T}$ of gas and solids, drag D, and heat transfer Q.

The gas phase stress is modeled as

$$\mathbf{T}_g = \varepsilon_g\mu_{ge}2\boldsymbol{\tau}_g \tag{9}$$

where

$$\boldsymbol{\tau}_g = \tfrac{1}{2}(\nabla\mathbf{v}_g + (\nabla\mathbf{v}_g)^T) - \tfrac{1}{3}(\nabla\cdot\mathbf{v}_g)\mathbf{I} \tag{10}$$

In above equations the superscript T denotes the mathematical operation of transpose, $\mathbf{I}$ is the unit tensor, and μ_{ge} is an effective viscosity of gas that includes the turbulence effects. The effective gas viscosity can include contributions from the molecular and turbulent effects of the gas phase as well

as the effects from the presence of particles in the flow field. For very low values of ε_s ($<10^{-6}$) the particles have a negligible effect on gas turbulence. For $10^{-6} \leq \varepsilon_s < 10^{-3}$, however, the volumetric particle loading is large enough to begin altering the turbulence structure, such that large particles lead to turbulent energy production and small particles lead to turbulent energy dissipation. When $\varepsilon_s > 10^{-3}$, the particle-particle collisions take place and a two-way coupling between the gas and particle turbulence should be expected [*Crowe*, 1982]. In the present model we will, however, ignore the effects of particles modulating the gas turbulence and model the effective gas viscosity using a turbulent subgrid scale model according to which

$$\mu_{ge} = \mu_g + \mu_{gt} = \mu_g + 0.01\Delta R\Delta Z\rho_g(2tr(\tau_g\tau_g))^{1/2} \quad (11)$$

where μ_g is the molecular viscosity of gas and tr denotes the trace operation. The adopted turbulent viscosity model simulates the local Reynolds stresses over the finite difference grid volume $R\Delta\theta\Delta R\Delta Z$ which is involved in the numerical simulation. It has proved successful in the modeling of jets in pulverized coal combustors and fluidized beds [*Fan et al.*, 1985]. The thermal conductivity in the energy equation (7) is assumed to be constant or to represent an effective value when the flow is turbulent.

The solids phase stress is modeled with a kinetic theory model of granular flow according to which

$$\mathbf{T}_s = -(P_s - \varepsilon_s\xi_s\nabla\cdot\mathbf{v}_s)\mathbf{I} \quad (12)$$

The solids pressure P_s and solid phase bulk viscosity ξ_s are found from

$$P_s = \varepsilon_s\rho_s[1 + 2(1+e)\varepsilon_s g_0]T_K \quad (13)$$

$$\xi_s = \frac{4}{3}\varepsilon_s\rho_s d_s(1+e)g_0\left(\frac{T_K}{\pi}\right)^{1/2} \quad (14)$$

where e is the restitution coefficient involved in the particle collisions, d_s is the particle diameter, g_0 is the radial distribution function, and T_K is the granular temperature. The radial distribution function of *Ogawa et al.* [1980] adequately models granular flows and has the following form:

$$g_0 = \left[1 - \left(\frac{\varepsilon_s}{\varepsilon_{sM}}\right)^{1/3}\right]^{-1} \quad (15)$$

where ε_{sM} is the maximum volumetric solids fraction possible in a flow. The uniform size spheres have a maximum solids fraction $\varepsilon_{sM} = \pi/(3(2^{1/2})) = 0.74$, whereas for a random packing, $\varepsilon_{sM} \approx 0.64$ and gives a closer agreement of predicted stresses with experiments [*Jenkins and Savage*, 1983]. The granular temperature is determined by solving the following transport equation of the kinetic theory:

$$\frac{3}{2}\left[\frac{\partial}{\partial t}\varepsilon_s\rho_s T_K + \nabla\cdot(\varepsilon_s\rho_s\mathbf{v}_s T_K)\right] = tr(\mathbf{T}_s\nabla\mathbf{v}_s) + \nabla\cdot\kappa\nabla T_K - \gamma \quad (16)$$

In this equation, κ denotes the conductivity of the particle fluctuation energy giving rise to the granular temperature, whereas γ is a collisional energy dissipation function. It should be noted that the transport equation (16) neglects the effect of the gas phase turbulence on the particle fluctuations and can be justified for large and heavy particles that are typical of some volcanic eruptions. (The effect can be either a production or a dissipation term of the particle fluctuation energy, and a corresponding term should be included in the fluctuation energy equation of the gas phase to account for turbulence modulation of gas by particles in a more sophisticated turbulence modeling approach.) Conductivity κ and the energy dissipation function γ are given by

$$\kappa = 2\rho_s\varepsilon_s^2 d_s(1+e)g_0\left(\frac{T_K}{\pi}\right)^{1/2} \quad (17)$$

$$\gamma = 3(1-e^2)\varepsilon_s^2\rho_s g_0 T_K\left[\frac{4}{d_s}\left(\frac{T_K}{\pi}\right)^{1/2} - \nabla\cdot\mathbf{v}_s\right] \quad (18)$$

The drag between the gas and solids can be expressed as [*Wallis*, 1969]

$$D = \frac{3}{4}C_d\frac{\varepsilon_g\varepsilon_s\rho_g|\mathbf{v}_g - \mathbf{v}_s|}{d_s}\varepsilon_g^{-2.7} \quad (19)$$

where the drag coefficient C_d is given by

$$C_d = \frac{24}{Re_s}[1 + 0.15\,Re_s^{0.687}] \qquad Re_s < 1000$$
$$C_d = 0.44 \qquad Re_s \geq 1000 \quad (20)$$

$$Re_s = \frac{\varepsilon_g\rho_g d_s|\mathbf{v}_g - \mathbf{v}_s|}{\mu_g} \quad (21)$$

The heat transfer between the phases is modeled by an empirical correlation [*Wakao et al.*, 1979] which accounts for the convective energy exchange but neglects the radiative heat transport processes which are generally negligible in comparison to the convective heat transfer [*Valentine and Wohletz*, 1989*a*]. Thus

$$Q = Nu\frac{6k_g\varepsilon_s}{d_s^2} \quad (22)$$

where

$$Nu = (2 + 0.16\,Re^{0.67}) \qquad Re \leq 200$$
$$Nu = 8.2\,Re^{0.6} \qquad 200 < Re \leq 1000$$
$$Nu = 1.06\,Re^{0.457} \qquad Re > 1000 \quad (23)$$

$$Re = \frac{\rho_g d_s|\mathbf{v}_g - \mathbf{v}_s|}{\mu_g} \quad (24)$$

Finally, it is assumed that the gas and solids form a saturated two-phase mixture whereby

$$\varepsilon_s + \varepsilon_g = 1 \quad (25)$$

The mole fractions x_w and x_a and mass fractions y_w and y_a must also satisfy the conditions

$$x_w + x_a = 1, \qquad y_w + y_a = 1 \quad (26)$$

The mole fraction of water vapor is equal to its volumetric fraction in the gas phase because of the ideal gas law assumption (see below). In the paper the water vapor mole

TABLE 1. Physical Properties and Parameters Employed in the Model

Physical Property	Value
μ_g, Pa s	10^{-5}
k_g, W/m K	0.05
k_s, W/m K	2.2
ε_M	0.64
e	0.9
Cp_a, m^2/s^2 K	$(6 + 0.002T_g - 0.3 \times 10^{-6} T_g^2) \frac{4.18 \times 10^3}{28.964}$
Cp_w, m^2/s^{2}K	$(8 + 0.0015\, T_g + 0.13 \times 10^{-5}\, T_g^2) \frac{4.18 \times 10^3}{18}$
Cp_s, m^2/s^2 K	1.3×10^3

fraction therefore will be referred to as the water vapor volumetric fraction.

In the model above, the effect of water vapor condensation is ignored. This effect can be incorporated readily in the modeling equations and appears to be very important after several minutes in the studied eruption columns. Whenever the vapor condensed, or the partial pressure of vapor in the mixture of water vapor and air became greater than the saturation pressure of vapor at the same temperature, the numerical simulation was terminated as further discussed below.

Equations of State and Physical Property Data

It is assumed in the above model that the gases obey the ideal gas law

$$P_g = \rho_g \bar{R} T \tag{27}$$

where $\bar{R}$ is the gas constant of a mixture of water vapor and dry air and is determined from the mole fractions x_w and x_a and molecular weights M_w and M_a, i.e.,

$$\bar{R} = \frac{\mathcal{R}}{x_w M_w + x_a M_a} \tag{28}$$

$\mathcal{R}$ is the universal gas constant, M_w = 18 kg/kg mol, M_a = 28.964 kg/kg mol, and x_w and x_a can be determined from the mass fractions y, that is,

$$x_n = \frac{y_n}{M_n} \frac{1}{\dfrac{y_w}{M_w} + \dfrac{y_a}{M_a}}, \qquad n = w, a \tag{29}$$

The temperatures of gas T_g and solid particles T_s are determined from

$$T_g = \frac{h_g}{Cp_g}, \qquad T_s = \frac{h_s}{Cp_s} \tag{30}$$

where the specific heat of solids Cp_s is assumed constant and that of gas is determined from

$$Cp_g = y_w Cp_w + y_a Cp_a \tag{31}$$

Table 1 summarizes the physical property and parameters data that were used to complete the physical model. This information together with data given in Table 2 that are specific to the studied eruptions were employed in the simulations reported in the paper.

Initial and Boundary Conditions

The solution of the conservation and balance equations discussed above depends on the initial conditions of the atmosphere into which a two-phase volcanic jet of gases and pyroclasts is discharging from a vent. For an assumed axisymmetric flow configuration above a volcanic vent as depicted in Figure 1, the initial conditions in the physical domain with radial extent L and vertical height H are assumed to correspond to the standard atmosphere which has a vertical temperature and pressure stratification. The boundary conditions at the axis of symmetry demand that the radial gradients of all dependent variables in the model be zero. At the impermeable wall at Z = 0, the no-slip condition of radial gas velocity is assumed, and no mass and heat transfer are allowed. The radial solids velocity along the wall is assumed, however, to slip according to the kinetic theory relation [*Eldighidy et al.*, 1977], that is,

$$u_s|_{wall} = \lambda_s \left(\frac{\partial u_s}{\partial Z}\right)_{wall} \tag{32}$$

where the slip parameter λ_s can be assumed to be the mean distance between particles and can be estimated from

$$\frac{\pi}{6} d_s^3 = \varepsilon_s \frac{\pi}{6} \lambda_s^3 \tag{33}$$

or

$$\lambda_s = \frac{d_s}{\varepsilon_s^{1/3}} \tag{34}$$

Notice from these equations that as the particle diameter becomes small the boundary condition of the radial solids velocity approaches the no-slip condition. The boundary condition for the granular temperature or fluctuating particle

TABLE 2. Geometry and Two-Phase Flow Conditions of Gas and Pyroclasts at Volcanic Vents of Eruptions Used in the Numerical Simulations

Eruption	D_v, m	T_v, K	v_v, m/s	P_v, MPa	ε_{sv}	y_{wv}	ρ_s, kg/m^3	d_s, μm	$\dot{m}$, kg/s	ρ_{mv}, kg/m^3	Z_c, m
A	100	1120	56	0.1	0.0754	1	2400	200	8×10^7	181	150
B	600	1200	200	0.1	0.01	1	2300	10	1.3×10^9	23	1700
C	600	1200	250	0.1	0.005	1	2300	10	8.3×10^8	12	3400

At the vent the phases are assumed to be in thermal and mechanical equilibrium. The discharge rates and mean densities at the vents were computed from the independent parameters in the table, whereas the fountain heights were obtained from the numerical results.

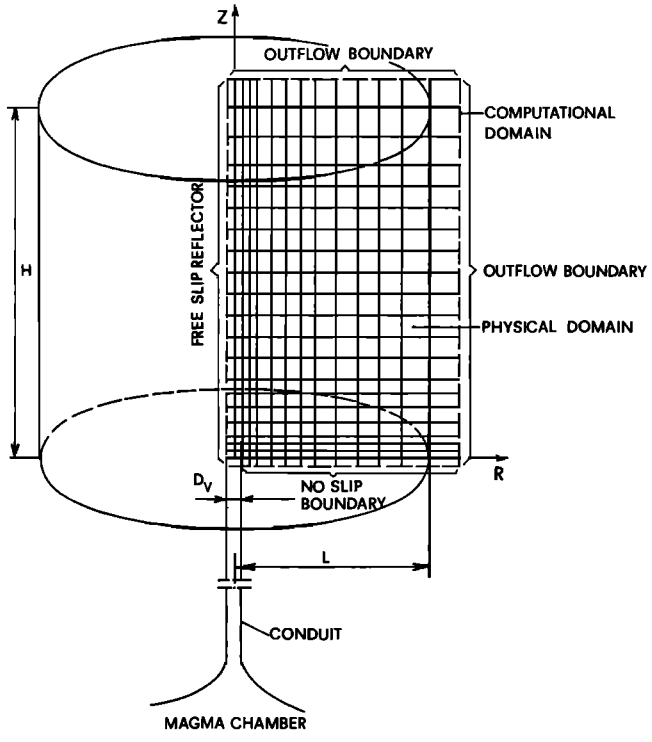

Fig. 1. Schematic illustration of the physical and computational domains in an axisymmetric flow configuration above a volcanic vent. A two-phase flow mixture of water vapor and pyroclasts (solid particles) exits from a vent of diameter D_v and mixes with the pressure and temperature stratified atmosphere above the vent. The physical domain has a radial extent L and a vertical extent H. The computational domain is two cells wider than the physical domain in the radial and vertical extents. The description of different types of boundaries employed in the numerical solution procedure is also shown.

velocity at the impermeable wall is assumed to correspond to the adiabatic condition or zero granular temperature gradient. At the outlet boundaries (see Figure 1) the pressure, mass, and energy fluxes are assumed to be continuous, whereas at the vent the solids volumetric fraction, water vapor mass fraction, pressure, and gas and solids velocities and temperatures are assumed to be given. The granular temperature at the vent is assumed to be equal to zero.

Numerical Solution Procedure

For an axisymmetric flow configuration as depicted in Figure 1, the modeling equations (1)–(8) and (16) compose a set of 11 partial differential equations that were numerically solved by the finite difference algorithm of *Harlow and Amsden* [1975]. The numerical procedure discretizes the partial differential equations on a staggered grid and treats pressure and drag terms in the momentum equations implicitly. An iterative procedure for pressure is then employed in order to satisfy the conservation of mass equations within a prescribed mass residual. After solving the momentum and mass balance equations, the gas and solids enthalpies are solved explicitly and the gas and solids temperatures implicitly from the temperature-dependent specific heats. The gas density is then updated employing the equation of state.

Because of the nonfully implicit time differencing, the numerical stability places a limitation on the time step size in each computational cycle. This time step must be small enough to preclude the material motion across a computational cell within the cycle. Such a condition is satisfied in the adopted numerical approach if

$$\Delta t < 0.2 \frac{\Delta Z_{min}}{v_M} \tag{35}$$

where Δt is the time step, ΔZ_{min} is the smallest cell dimension, and v_M is the largest flow velocity that normally can be assumed to occur at the vent.

The accuracy considerations also impose limitations on cell size and time step per cycle. Very fine cell sizes provide more accurate results and demand very small time steps, which in turn may require very long or unacceptable computing times. In testing the numerical procedure and adequacy of the physical model, different grid sizes and computational domains, time steps, and mass residuals were employed. The mass residual which expresses an error associated with the violation of the conservation of mass of each phase and for each cell size, was changed until it produced no noticeable differences in results, and all computations were carried out in double precision arithmetic. The time steps varied from 0.025 to 0.2 s, depending on the grid size. The numerical results were subsequently postprocessed by a computer program which transformed the variables computed on the staggered grid onto the regular grid points of the physical domain by employing two-dimensional interpolation. The postprocessed data were subsequently used to generate the graphical results.

RESULTS

Several collapsing volcanic columns were simulated with different mesh and computational domain sizes. In this section some results of these simulations will be presented and discussed mainly to ascertain the validity of the modeling approach and numerical solution procedure. The application of the model to historic volcanic eruptions and a more detailed study of pyroclastic flows is in progress and will be reported in the future.

A summary of the vent geometry and two-phase flow conditions of gas and pyroclasts of three different volcanic eruptions are shown in Table 2. Eruption A is similar to the eruption of Vesuvius in A.D. 79, with the difference that the latter eruption contained much more water vapor [see *Dobran*, 1992] than did eruption A. Because of the large content of pyroclasts, the column of eruption A forms a fountain at about 150 m above the vent and produces a radially spreading pyroclastic flow and a co-ignimbrite-type column above the flow. Eruptions B and C in Table 2 are physically similar to eruption A, except that they are very large scale eruptions that form fountains several kilometers above the vents, produce thick pyroclastic flows, and may produce fountain height oscillations. For each of these eruptions a convergence study was also carried out to assess the adequacy of the employed cell and computational domain sizes in the numerical calculations.

Eruption A

Volcanic eruption A was simulated on a physical domain involving L = 10 km and H = 2.4 km and comprised a nonuniform cell size: beginning with 10 m in radial direction

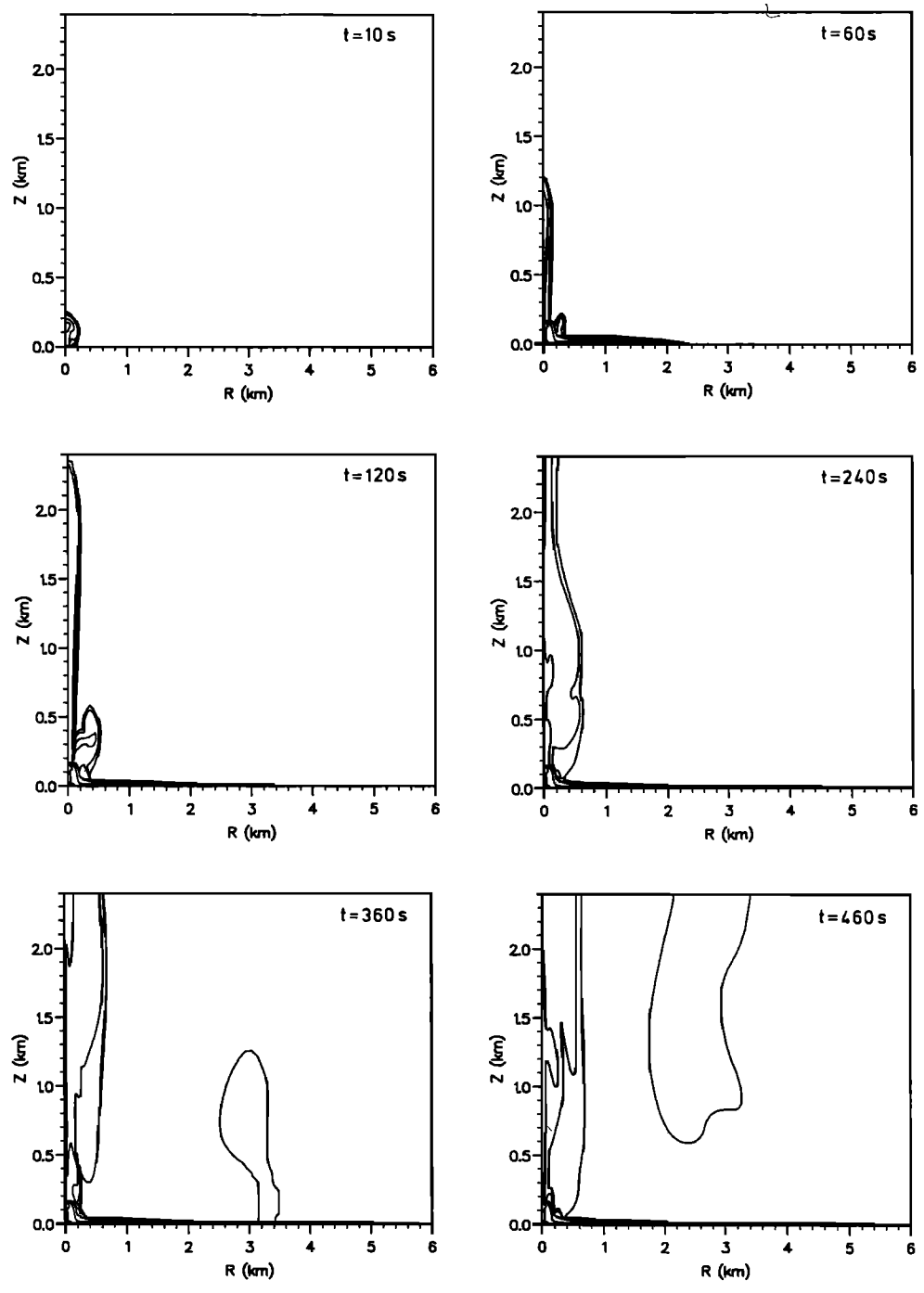

Fig. 2. Distribution of particulate volumetric fraction in the atmosphere at 10, 60, 120, 240, 360, and 460 s of eruption A. The contour levels shown are the exponents to the base 10 and, beginning from the outer or distant from the vent region, correspond to −10, −8, −6, −4, −2, and −1. The contour level of the co-ignimbrite cloud corresponds to 10^{-10}.

until 1 km and thereafter increasing 10 m every four cells until reaching a cell width of 120 m. In the vertical direction the cell size started with 10 m until a height of 400 m and thereafter increased by 10 m every four cells until reaching a cell width of 100 m. The selection of these computational parameters was guided by the available computer memory, reasonableness in execution time, and preliminary computations to ascertain a satisfactory resolution of high flow gradients. The results from a convergence study are presented below, after discussing the results involving the above cell and computational domain sizes.

The distribution of the particulate phase volumetric fraction in the atmosphere at 10, 60, 120, 240, 360, and 460 s is illustrated in Figure 2, whereas the same timewise distribution of the water vapor volumetric fraction is shown in Figure 3. The contour levels in Figures 2 and 3, moving from the outer region toward the vent, correspond to 10^{-10}, 10^{-8}, 10^{-6}, 10^{-4}, 10^{-2}, 10^{-1}, and respectively. At about 10 s the

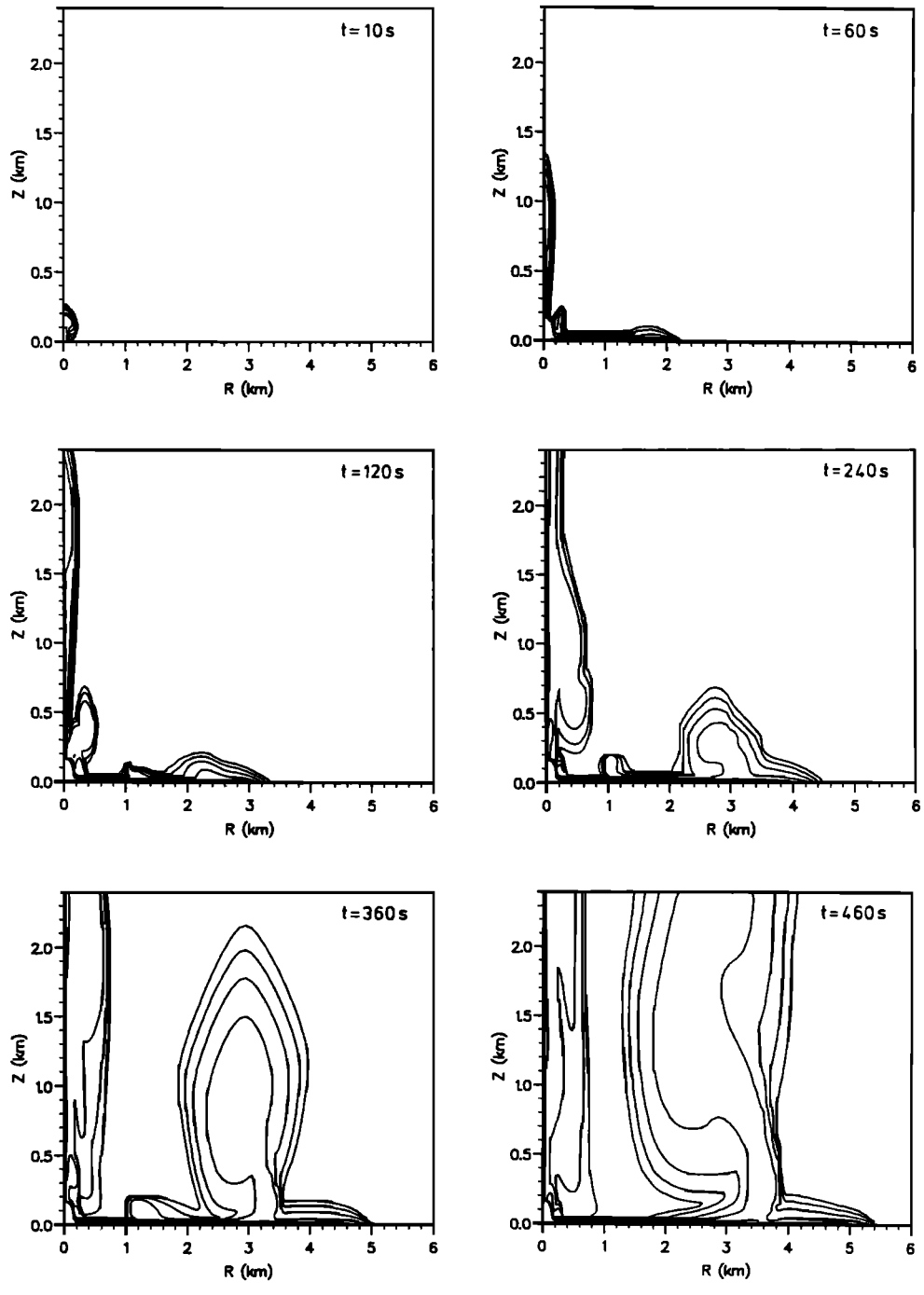

Fig. 3. Distribution of the water vapor volumetric fraction in the atmosphere at 10, 60, 120, 240, 360, and 460 s of eruption A. The contour levels shown are the exponents to the base 10 and, beginning from the outer or distant from the vent region, correspond to −10, −8, −6, −4, −2, −1, and 0.

high-momentum jet losses its vertical thrust at about 170 m above the vent by forming a fountain and initiating the column collapse. Above the fountain the rising water vapor entrains some particles and continues to rise as a dilute buoyant cloud. The collapsed column forms a radially spreading pyroclastic flow that reaches a distance of about 5.5 km after 460 s. At about 120 s the high-temperature water vapor and small quantities of ash (corresponding to a particle volumetric fraction less than 10^{-8}) separate from the pyroclastic flow and begin forming a co-ignimbrite plume or "phoenix" column at about 3 km from the vent. (Calling the co-ignimbritic column the "phoenix" column is appropriate since this column rises from its own ashes as the fabled bird in mythology.) Figure 3 illustrates how this column forms very rapidly and tends to join the column above the fountain at about 8 min. The computation was terminated after this time due to the water vapor condensation in the column above the fountain which was not included in the model. As further discussed below, the phoenix column forming above the pyroclastic flow is due to the diminishing radial momentum of the flow which leads to the particle sedimentation along the ground and mean density decrease in the upper

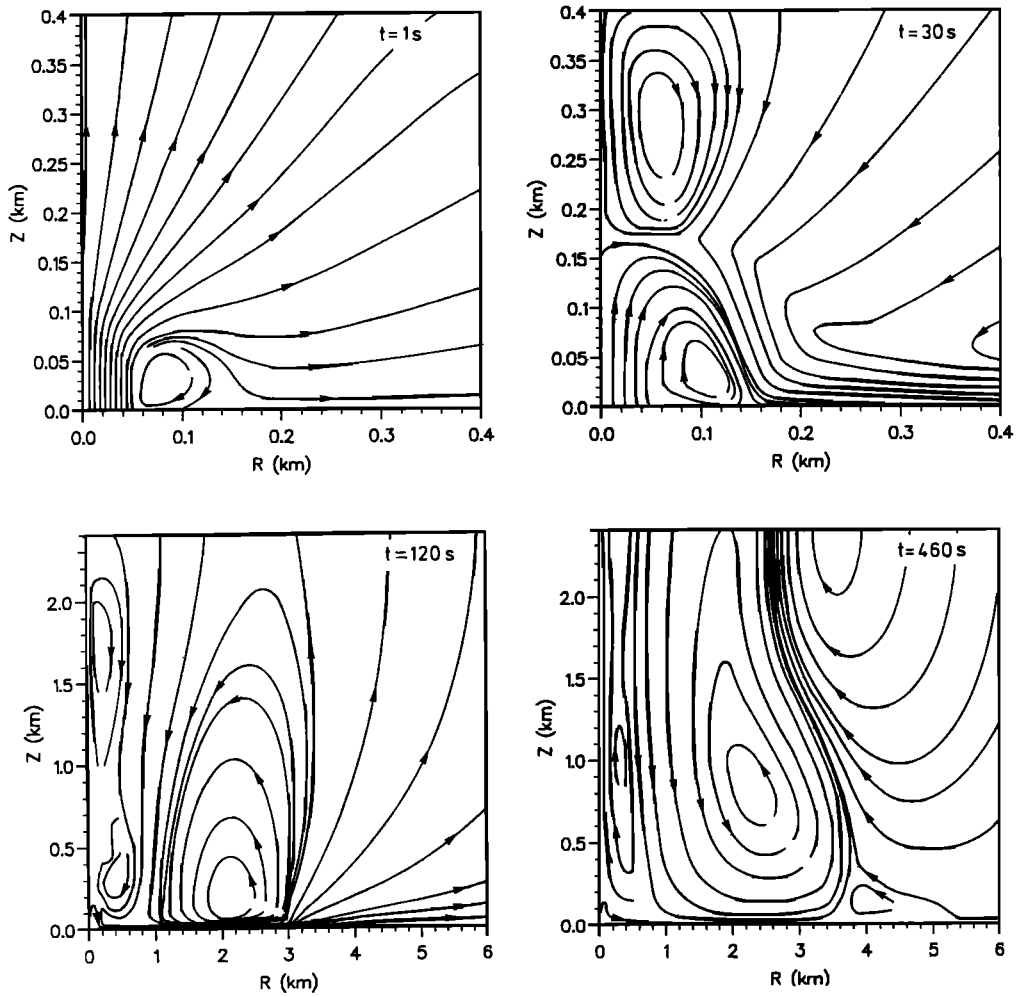

Fig. 4. The gas streamline patterns of eruption A at 1, 30, 120, and 460 s. The streamline patterns of particles are similar. Several interesting flow patterns emerge: recirculation of the material from the column back into the fountain, entrainment of air into the column above the fountain and into the radially spreading pyroclastic flow, development of large recirculatory flow structures above the fountain and pyroclastic flow, and necking of the co-ignimbrite cloud above the flow.

layers of the flow and creation of an unstable density gradient. It can also be seen from Figures 2 and 3 that the pyroclastic flow travels at about 40 m/s before and at about 10 m/s after the formation of the co-ignimbrite cloud. Although the particle volumetric fractions up to 10^{-10} are shown in Figure 2, such levels do not appear to be observable. The photographs of volcanic clouds show that their edges or opacity are very well defined; this seems to suggest the existence of steep gradients of dust and/or water droplet loading at the edges. In the absence of water vapor condensation which produces a white cloud, it is difficult to place a limit on ε_s which produces a cloud observability. However, from the observations of dust storms [*Chepil and Woodruff*, 1957] it appears that this limit can be taken as $\varepsilon_{smin} = 10^{-8}$ for 20-μm particles when observed from a distance of about 1 km.

The gas streamline patterns are illustrated in Figure 4 at times of 1, 30, 120, and 460 s. At 1 s the volcanic jet penetrates into the atmosphere and entrains air into the jet close to the vent. At 30 s the collapsed column produces a radially propagating pyroclastic flow, a recirculatory motion above the fountain, entrainment of air toward the fountain and into the pyroclastic flow and cloud above the fountain, and a recirculation of the jet material into the fountain. Large recirculation zones are clearly visible above and near the fountain at 120 s, and at 460 s the pattern above the pyroclastic flow and fountain has changed owing to the formation of a co-ignimbrite cloud which produces an inward necking effect due to the fast rising plume. A more detailed illustration of the gas and particle motions near the vent is depicted in Figure 5 at 120 s. Of special interest in Figure 5 is the relative velocity between the gas and particles. Above the vent, both the particles and gas are slowed down owing to the atmosphere which tends to compress the gas-particle mixture toward the vent (see below and Figure 9 for more detailed explanation). Because of the large inertia of particles, however, they tend to decelerate more slowly and move faster than the gas, as do the particles hitting the ground from the collapsed column (at about 150 m radially from the vent). The particles also hit the ground at a steeper angle than does the gas.

An important test of the model and computational procedure is reflected in the excellent prediction of the propagation of acoustic waves in the atmosphere during the initial

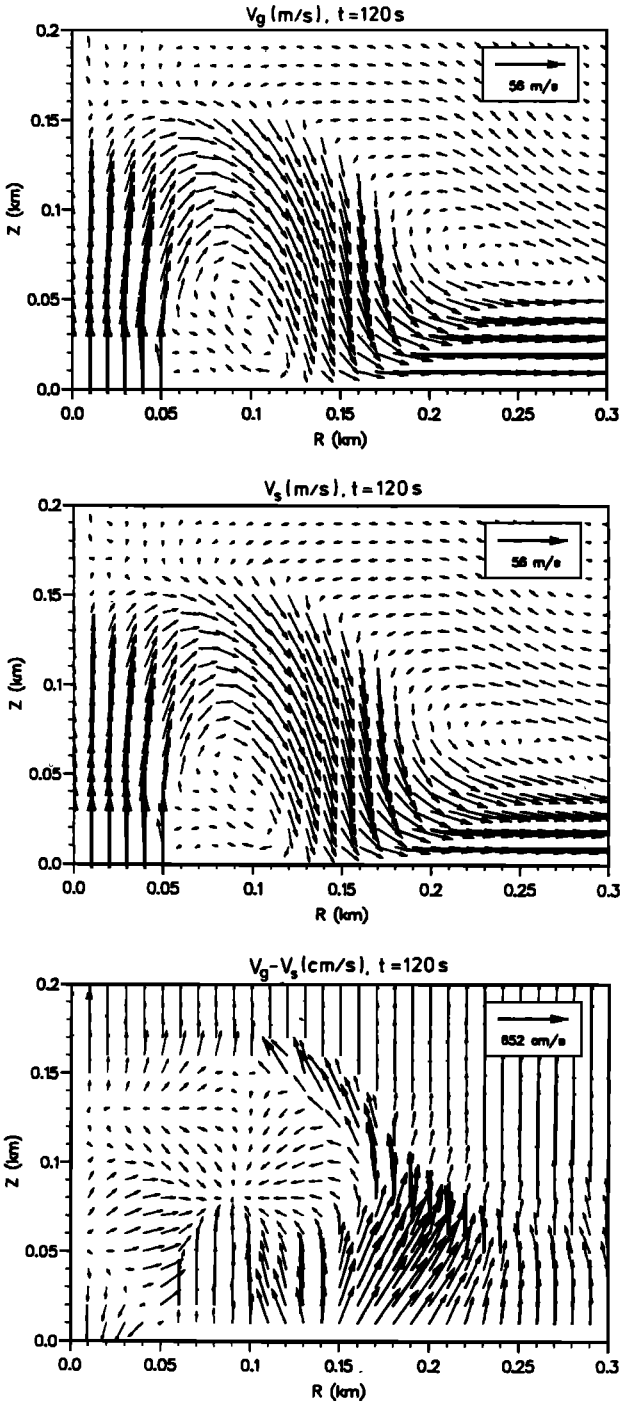

Fig. 5. The gas, particle, and difference between the gas and particle velocity vector plots of column A at 120 s in the fountain. The velocity difference vector plot shows how the particles move faster than the gas immediately above the vent and in the region where the column hits the ground. The maximum flow velocity is reported in the inserts.

times of transient when these waves are contained within the computational domain. Figure 6 illustrates the overpressure (difference between the actual pressure and the atmospheric pressure at the same vertical position but at large radial distances from the symmetry axis) contours in pascals in the atmosphere at 1, 3, 5, and 8 s. During the first few seconds the sound wave propagates spherically above the thrusting volcanic jet, and after about 5 s it interacts with and reflects from the impermeable boundary. The speed of propagation of the acoustic wave can be estimated at 270 m/s, which compares favorably with a value of about 300 m/s at 1500 m height in the standard atmosphere.

The thrusting volcanic jet and evolution of the fountain contain interesting physics. Figures 7, 8, and 9 illustrate this evolution with plots of pressure, mixture density of gas and pyroclasts, vertical component of gas velocity, fountain height, and Mach number. The distributions of pressure, mixture density computed from

$$\rho_m = \varepsilon_s \rho_s + (1 - \varepsilon_s)\rho_g \tag{36}$$

and vertical gas velocity with height and at different radial distances from the vent are shown in Figure 7 at 3 s during the jet thrusting, at 13 s during the lateral spreading and column collapse, at 30 s when the column has collapsed and a quasi steady state height of the fountain achieved, and at 460 s during an apparent steady state condition of the fountain. The jet thrusting into the atmosphere produces a conversion of its kinetic energy into pressure and gravitational potential energy, which compresses the mixture to a maximum pressure and density. Above this maximum in pressure and density, the pressure is converted into the gravitational potential energy with the kinetic energy further loosing its initial importance. After the column collapse, the pressure and density distributions degenerate into a two-pressure peak with the maximum located well within the fountain. Figure 7 also shows that the maxima in mixture density at the axis of symmetry correspond to the nearest local maxima in pressure, whereas the minima of vertical gas (and mixture) component of the velocity along the axis are located above these pressure and density maxima. Because of this complex dynamics it is not clear how to define a suitable fountain height Z_c. For this purpose, Figure 8 illustrates timewise plots of different fountain heights that correspond to maximum pressure near the top of the fountain (points labeled A in Figure 7), pressure equal to atmospheric above the fountain (points A′ in Figure 7), maximum density in the fountain (points B in Figure 7), and density equal to atmospheric near the top of the fountain (points B′ in Figure 7). (The points A, A′, B, and B′ are also plotted in the vertical velocity plots in Figure 7.) The maximum pressure at the symmetry axis reaches a value of 0.22 MPa at 13 s and Z = 120 m, but this maximum in pressure does not correspond to the maximum height reached by the fountain. The maxima in pressure and density lag the maxima of fountain heights of about 6 s. This effect is due to the initial thrusting of the jet which produces a fountain at a maximum height. The material at this fountain height subsequently becomes too heavy to be supported by the jet and falls downward, where the thrusting pressure of the jet can support the column with a large density at a lower fountain height. At later times the fountain height is determined by the balance between the forces of the thrusting volcanic jet and the weight of the column material. The steady state fountain height which is based on the atmospheric density and pressure corresponds to 170 m, whereas the heights based on maxima in pressure and density are lower by about 30 m and correspond to 140 m. During the quasi steady state conditions in the fountain, the heights labeled with points A′ and B′ in the velocity plots in Figure 7 give a near-zero value of the vertical gas velocity at the symmetry axis. The

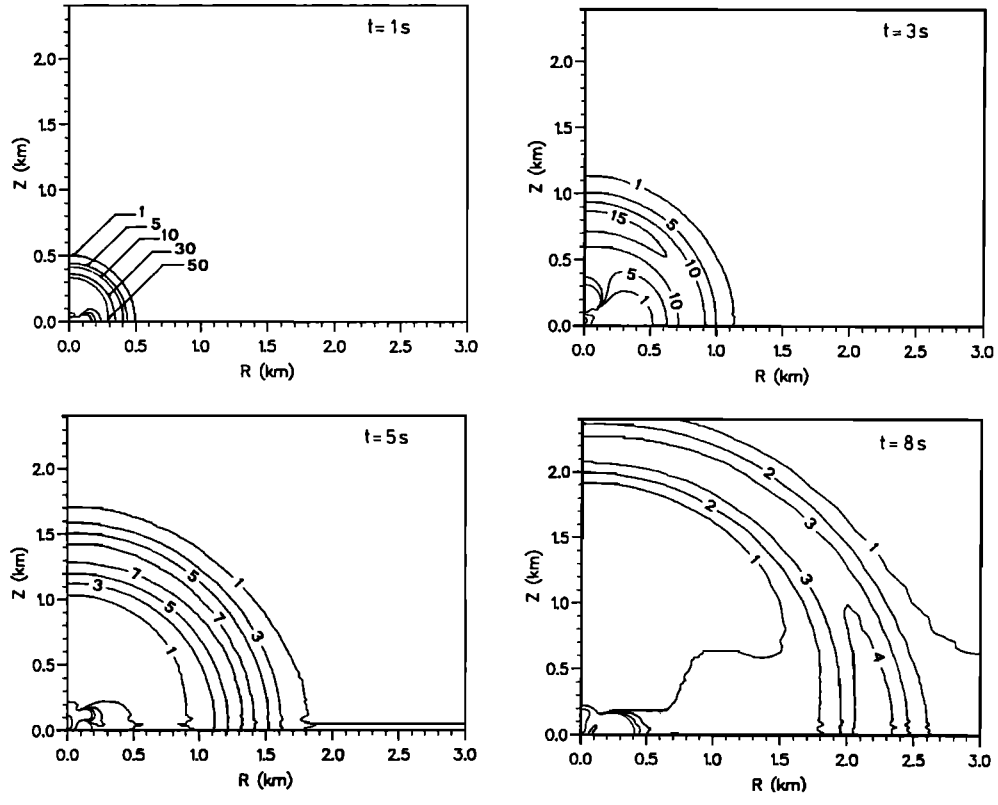

Fig. 6. Propagation of the acoustic wave in the atmosphere of eruption A at 1, 3, 5, and 8 s. This wave speed corresponds to approximately 270 m/s. At 8 s one may note the effect of the boundary on the wave propagation. An illustrated contour level represents the difference between the actual and the atmospheric pressures in pascals at the same vertical position. The pressure difference contours near the vent correspond to very large values and are not labeled.

collapse column height of $Z_c = 150$ m which is reported in Table 2 corresponds therefore to an average value.

It is instructive to compute an approximate value of the fountain height by a very simple model for comparison with the numerical predictions. Such a height can be estimated by selecting a stagnation streamline and assuming that the Bernoulli equation applies along it, that is,

$$Z_c = \frac{v_v^2}{2g} = \frac{56^2}{20} \approx 160 \text{ m} \tag{37}$$

The closeness of this result with the numerically predicted value of 150 m gives a further credibility to the adopted physical model.

The gas-particle mixture exiting from the vent of eruption A is in a supersonic flow with a Mach number of about 2. The Mach number can be computed from

$$\mathbf{M} = \frac{\mathbf{v}_m}{a} \tag{38}$$

where $\mathbf{v}_m$ is the mean flow velocity of gas and pyroclasts and a is the speed of sound of the mixture. The mean velocity is computed from

$$\mathbf{v}_m = \frac{\varepsilon_s \rho_s \mathbf{v}_s + (1 - \varepsilon_s)\rho_g \mathbf{v}_g}{\rho_m} \tag{39}$$

whereas the speed of sound can be established from a homogeneous flow approximation and ideal gas equation of state [*Wallis*, 1969], that is,

$$a = \left(\frac{\bar{R}T_g}{Y}\right)^{1/2}\left[Y + (1 - Y)\frac{\rho_g}{\rho_s}\right] \tag{40}$$

In this equation, Y is the mass fraction of gas in the two-phase mixture and can be computed from

$$Y = \frac{1}{1 + \dfrac{\varepsilon_s \rho_s}{(1 - \varepsilon_s)\rho_g}} \tag{41}$$

The numerical results show that most of the flow in the fountain, including a region of vent radius from the axis, is in supersonic flow. This prompted us to investigate more carefully the structural features of the flow by computing the normal Mach number M_n which is found from the mean velocity in the direction of pressure gradient. Thus

$$M_n = \frac{\mathbf{v}_m \cdot \nabla P_g}{a|\nabla P_g|} \tag{42}$$

Figure 9*a* shows the distribution of M_n at 1, 5, 15, and 30 s. At 1 s a weak shock appears at the radial and vertical distances corresponding to the vent radius. At 5 s an oblique

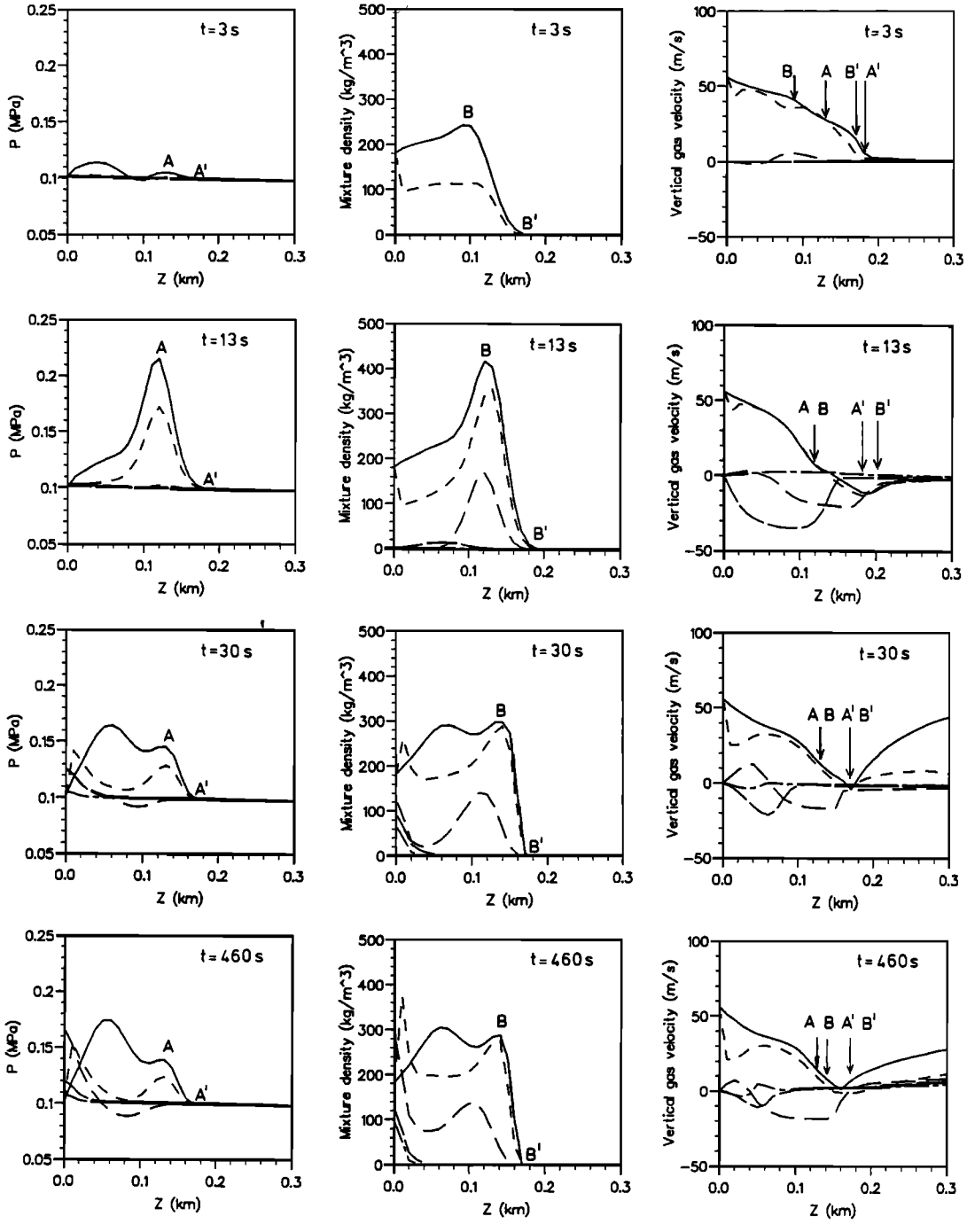

Fig. 7. Distributions of pressure, mean density, and vertical gas velocity of column A with height and several radial positions at 3, 13, 30, and 460 s. At approximately 13 s a fountain is formed, and lateral column collapse begins. The quasi steady state conditions in the fountain develop at about 30 s. The curves correspond to R = 0 km (solid line), R = 0.05 km (short-dashed line), R = 0.1 km (medium-dashed line), R = 0.2 km (long-dashed line), and R = 0.3 km (dot-dashed line).

weak shock is reflected from the symmetry axis, while at 15 s (time corresponding to the column collapse phase) it is detached from the axis. At 30 s the quasi steady state conditions in the fountain prevail, and the weak shock is shown reflecting from the axis again and appears to merge into a weak normal shock at about 90 m height. The numerical results based on the cell size of 10 m cannot of course resolve strong shocks, if they are indeed present, but only predict continuous property changes that may be associated with compression waves or weak shocks and rarefaction waves. Since the thrusting of the volcanic jet into the atmosphere produces higher pressures above and to the right of the vent (see Figure 7) than those at the vent, the flow must turn inward from the edge of the vent and produce compression waves as in an overexpanded nozzle flow where the exit plane pressure is lower than the surrounding atmosphere [*Liepmann and Roshko*, 1957]. These compression waves (waves *a* in Figure 9*b*) must subsequently reflect

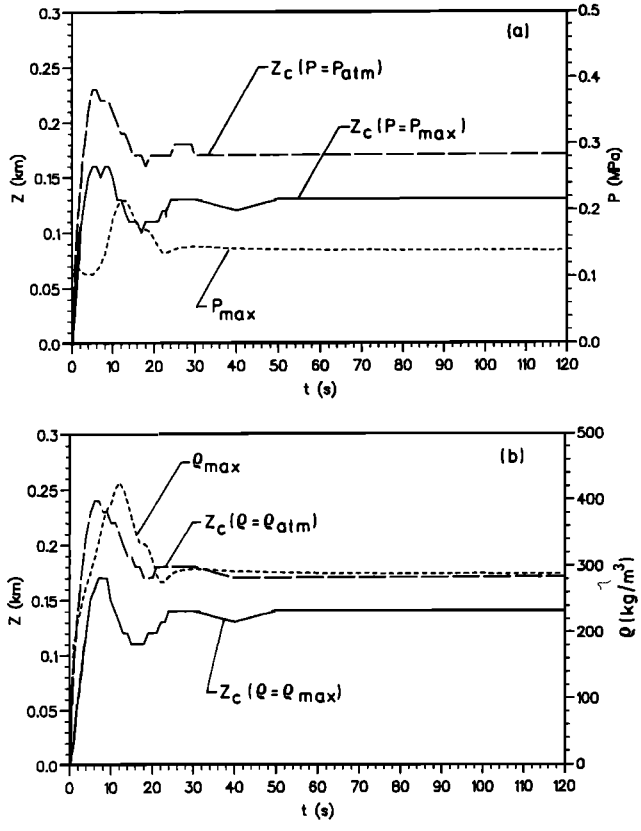

Fig. 8. Timewise distributions of fountain heights and maximum pressure and density in the fountain of eruption A. (*a*) Fountain heights corresponding to the maximum pressure near the fountain top and the pressure corresponding to atmospheric, all along the symmetry axis. The steady state heights correspond to about 170 and 130 m. (*b*) Similar distributions of mean density and the associated heights in the fountain. These steady state heights correspond to about 170 and 140 m.

from the symmetry axis as waves *b* in order for the flow not to cross the axis (as required by the conservation of mass) or for the flow directions to coincide in regions 1 and 3. The waves *b* do not, however, follow a regular reflection rule (angle of incidence of waves *a* is equal to angle of reflection of waves *b*), but a Mach reflection that at location C in the flow produce rarefaction waves *c*. The reflecting waves *b* can merge into a normal shock or produce expansion waves *c*. From a compressible flow analysis [*Liepmann and Roshko*, 1957] the weak shock turning angle δ is found from the Mach number in region 1 (Figure 9*b*) from

$$\tan \delta \approx \frac{1}{(M_1^2 - 1)^{1/2}} \tag{43}$$

which for $M_1 = 2$ gives $\delta = 30°$. This value is comparable with the value of about 45° in Figure 9*a*.

Some of the more interesting characteristics of the pyroclastic flow produced by eruption A include the conditions leading to the flow instability and the associated formation of the phoenix cloud above the flow. The employed computational cell size of 10 m close to the impermeable boundary proved to be effective in the understanding of the physical processes of the flow which forms a buoyant cloud between 2 and 4 km as may be seen from Figures 2 and 3.

The radial distributions of mixture density and gas temperature at several vertical positions in the pyroclastic flow and above the flow at 60, 120, 240, and 460 s are shown in Figure 10. The mixture density profiles illustrate the process of particle sedimentation in the flow whereby this density at first diminishes in radial direction and at about 2 km from the vent starts increasing to a large value, before decreasing to the atmospheric value at the pyroclastic flow front. The particle sedimentation process is very effective below the co-ignimbrite cloud, which is located between 2 and 4 km, and shows an increasing deposition of particles below the cloud with time. The gas at the impermeable wall cools very slowly, and at 10 m height its temperature is about 800 K, even after 460 s and 5 km from the vent. The gas below the rising phoenix cloud also exhibits local maxima and minima in temperature which is consistent with particle sedimentation. This local gas temperature increase results from the hot water vapor which is separated from the lower and hotter layers of the flow and which heats the upper layers as it rises buoyantly upward. The local gas temperature minima, or cooling of the flow, ahead of the maxima in Figure 10 are associated with air entrainment or inflow of cold air as a result of the vertically rising and necking of the co-ignimbrite cloud (see Figure 4).

The physics of formation of the co-ignimbrite cloud can be seen in Figure 11*a*, showing the vertical distributions of mixture density, gas density, and gas temperature at 120 s and at 2, 2.5, and 3 km from the vent. At 120 s the instability in the pyroclastic flow begins to form a column above the flow between 2 and 3 km (see also Figure 3). This instability is formed due to the diminishing radial momentum of the pyroclastic flow which subsequently produces particle separation from the gas phase and decrease of the mixture density in the upper layers of the flow. This mixture density decrease and the gas which moves buoyantly upward further contribute to the density decreases in the upper layers of the flow. This then creates an unstable density gradient that produces thermal convection and a rising cloud above the pyroclastic flow. Figure 11*b* illustrates the decrease of the horizontal component of gas velocity in the region of the phoenix column and the gas and particle velocity vector plots which show the effects of particle sedimentation and vertical transport of gas. The particle deposition ahead of the flow head is clearly visible, as is the gas which tends to rotate counterclockwise. In the velocity vector plots the velocities which are 100 times smaller than the maximum reported velocity in the box inserted in the figures are not shown. It should be noted that some particle velocities in Figure 11*b* correspond to very low values of the particle volumetric fraction, since the model solves the two-phase flow equations with particle volumetric fraction as low as $\alpha_p = 10^{-16}$.

Before selecting the above cell and computational domain sizes for the presentation of numerical results pertaining to eruption A, a convergence study was carried out involving these parameters. In this convergence study the range of cell sizes varied from 5 to 120 m in radial and vertical directions, with uniform and nonuniform distributions, whereas the computational domain sizes ranged from 4.8 to 10 km radially and from 0.9 to 20 km vertically. Figure 12 summarizes the effect of the cell size on the distribution of the particulate phase volumetric fraction at 60 and 120 s with a fixed computational domain of 0.9×4.8 km^2, uniform grid of 25 m, and nonuniform grids which start with cell sizes of

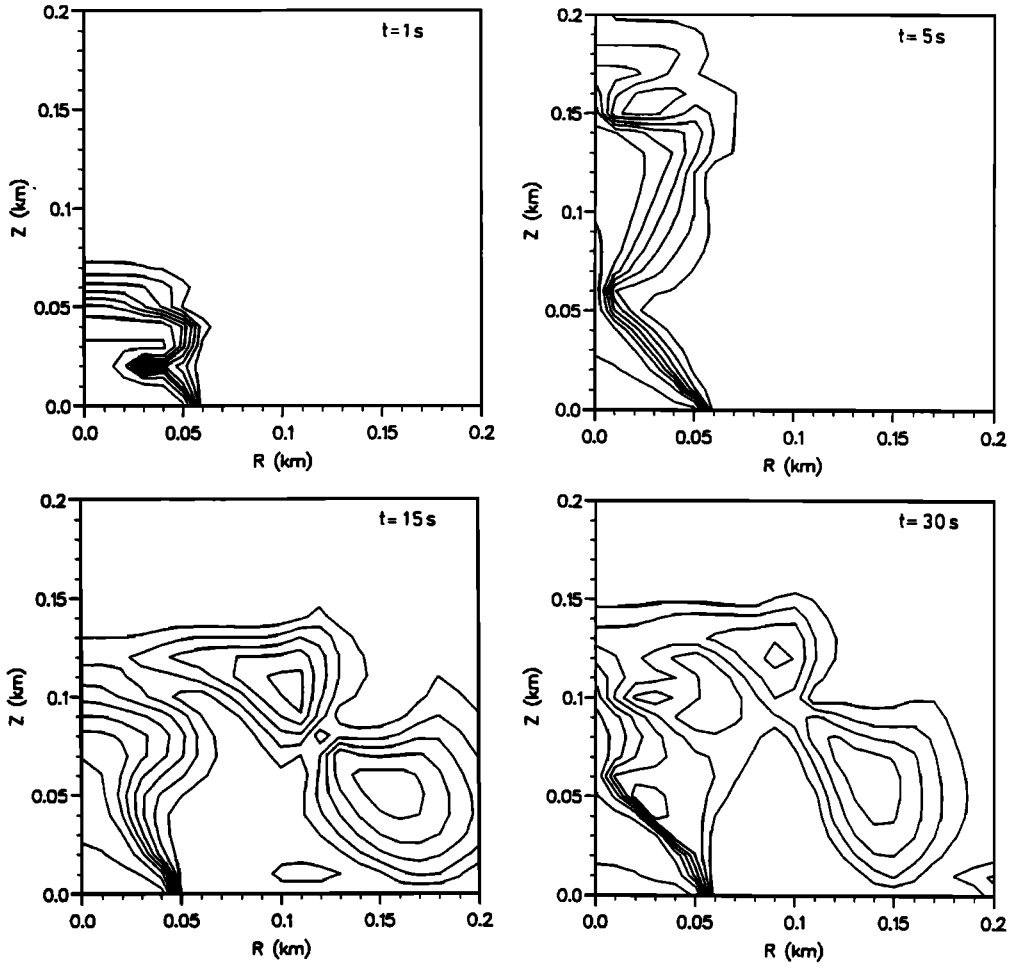

Fig. 9*a*. Normal Mach number distribution to 1, 5, 15, and 30 s near the vent of eruption A. The M_n contour lines close to the vent, beginning from the inner region, correspond to 2, 1.5, 1.2, 1, 0.8, 0.6, 0.4, and 0.2.

5 and 10 m. As shown in Figure 12, the effect of the cell size decrease from 25 to 5 m is to produce a reduction of the fountain height and thickness of pyroclastic flow, without affecting the global flow pattern. For high particle volumetric fractions, the cell size decrease increases the distance reached by the pyroclastic flow head, whereas for low particle volumetric fractions this conclusion is reversed. A similar analysis performed with different computational domains and time steps produced negligible effects on the fountain heights, pyroclastic flow thicknesses, and distances reached by the pyroclastic flow heads. It is clear from Figure 12, and in particular from Figure 12*b*, that the computational cell size has a significant effect on the results and that a cell size of 25 m is not acceptable for this column. This cell size produces a dispersion error which causes the material to pile up behind the front in an unphysical manner. A cell size of 10 m eliminates this dispersion error, but it still produces a difference in the pyroclastic flow thickness when compared with the results performed with a 5-m cell size. The latter cell size is too small to be used at present for performing practical volcanic simulations where one needs to understand the detailed properties of pyroclastic flows.

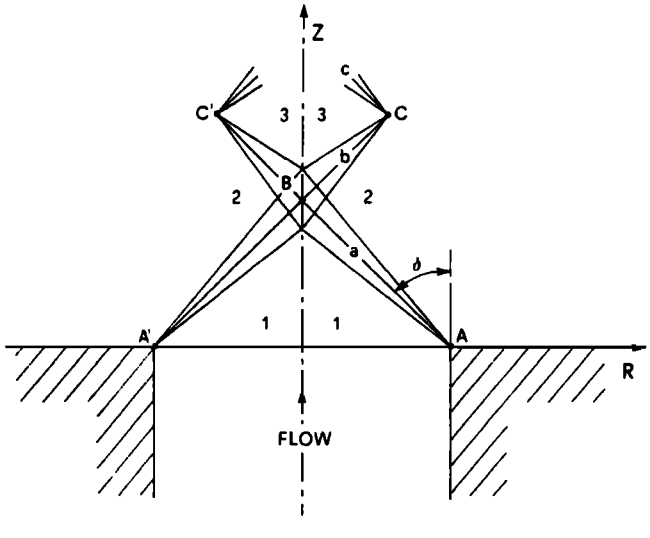

Fig. 9*b*. Interpretation of the flow pattern generated by compression and rarefaction waves in Figure 9*a*.

Eruption B

Eruption B (Table 2) is a very large scale volcanic eruption that may be typical of some past eruptions [*Walker*, 1981], such as Tambora (1815) [*Sigurdsson and Carey*, 1989; *Rampino and Self*, 1982] and Krakatau (1883) [*Self and Rampino*, 1981]. The eruption is produced by a vent diameter of 600 m,

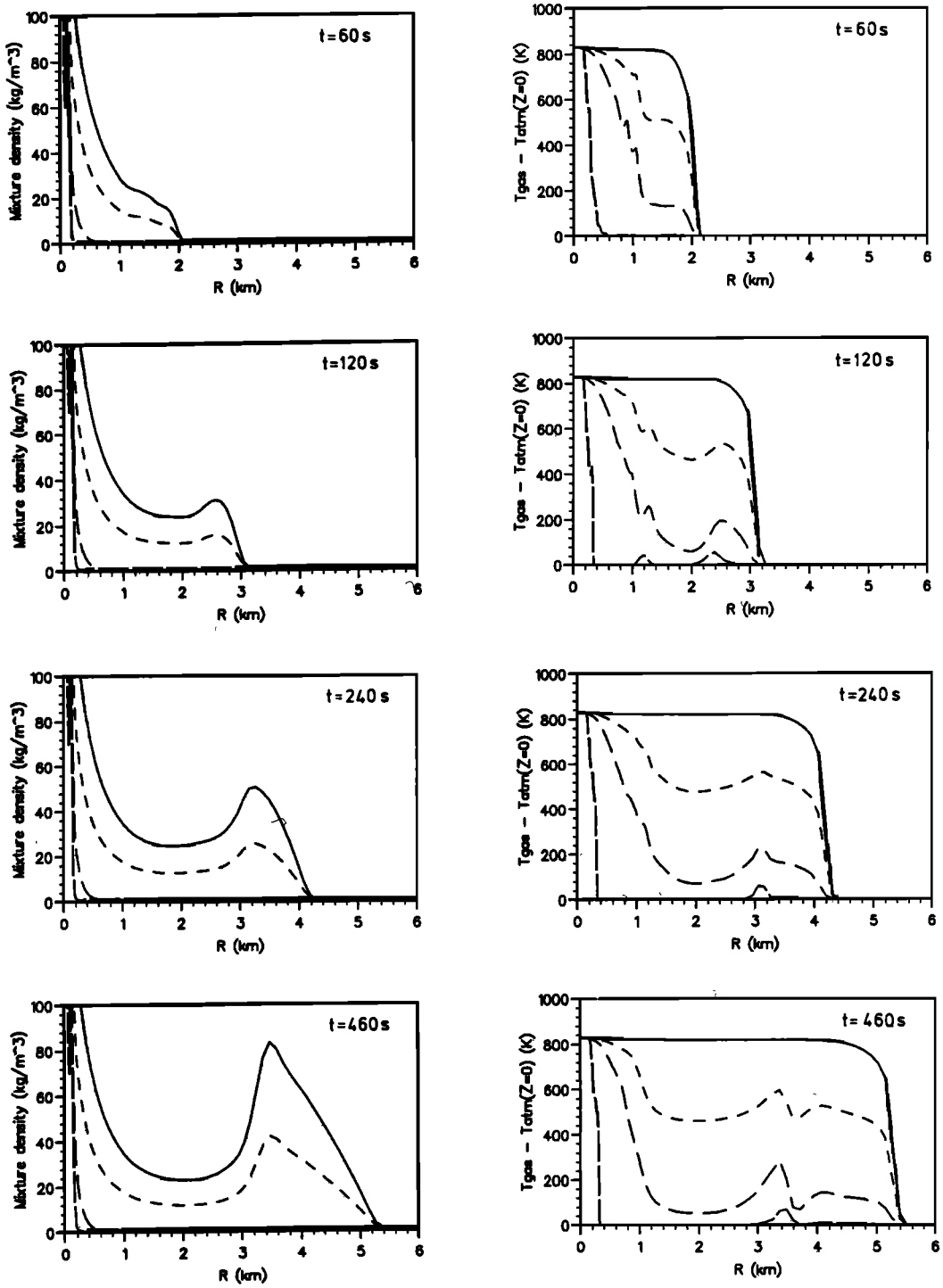

Fig. 10. Radial distributions of mixture density and temperature fronts at different heights in the pyroclastic flow of eruption A. The propagating fronts are shown at 60, 120, 240, and 460 s at heights of 0, 10, 20, and 50 m. Notice the particle sedimentation, high temperature of the flow, and local temperature maxima where the co-ignimbrite cloud forms. The local temperature minima ahead of maxima are due to the cooling effect of the entrained air. The curves correspond to Z = 0 km (solid line), Z = 0.01 km (short-dashed line), Z = 0.02 km (medium-dashed line), and Z = 0.05 km (long-dashed line).

gas and pyroclasts velocity of 200 m/s, particle volumetric fraction of 0.01, and particle diameter of 10 μm. The radial and vertical cell sizes and computational domain extents employed in the numerical simulations involved (1) a uniform cell size of 100 m on the computational domain of L = 12 and H = 20 km, (2) a uniform cell size of 50 m on L = 8 and H = 5 km, and (3) a uniform vertical cell size of 25 m and a nonuniform radial cell size starting from 25 m and increasing to 100 m on L = 8 and H = 5 km. The first simulation was carried out until 1100 s when the condensation of water vapor above the fountain terminated the computations. The second and third simulations were per-

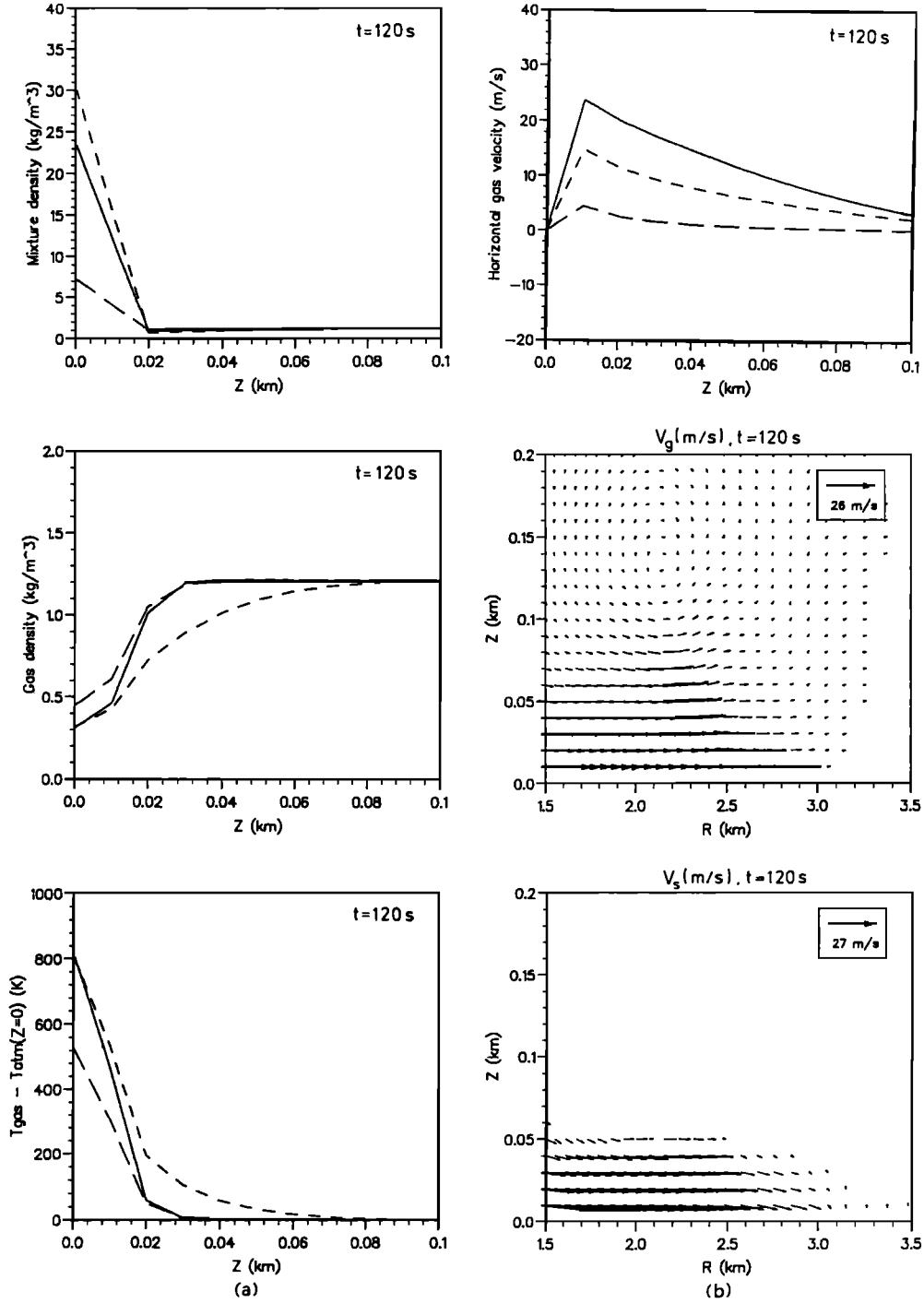

Fig. 11. Vertical distributions of densities, temperatures, and velocities of eruption A. (*a*) Mixture density, gas density, and gas temperature at 120 s and at 2, 2.5, and 3 km radially from the vent. (*b*) Vertical distribution of horizontal component of gas velocity, and the gas and particle velocity vector plots at 120 s. The vector plots show how the particles deposit in the pyroclastic flow head and how the gas rotates counterclockwise. The velocities that are 100 times less than the one reported in the inserts are not shown. The curves in the figure correspond to R = 2 km (solid line), R = 2.5 km (short-dashed line), and R = 3 km (long-dashed line).

formed up to about 550 s. Some results will be first presented from the simulation performed with a 100-m cell size to illustrate the large-scale effects of the eruption, before discussing results of a convergence study and simulations with smaller grid sizes.

For the first 30 s, eruption B builds a fountain at about 2000 m. It then spreads radially, collapses, and builds a pyroclastic flow. Above the collapsing column and fountain some particles are entrained in the rising water vapor and build a column that buoyantly rises. After about 300 s a column is formed at about 6 km from the vent on top of the pyroclastic flow, whereas at 1000 s almost all of the computational domain (12 × 20 km^2) is filled with a large quantity of water vapor, and cooling of the vapor produces conden-

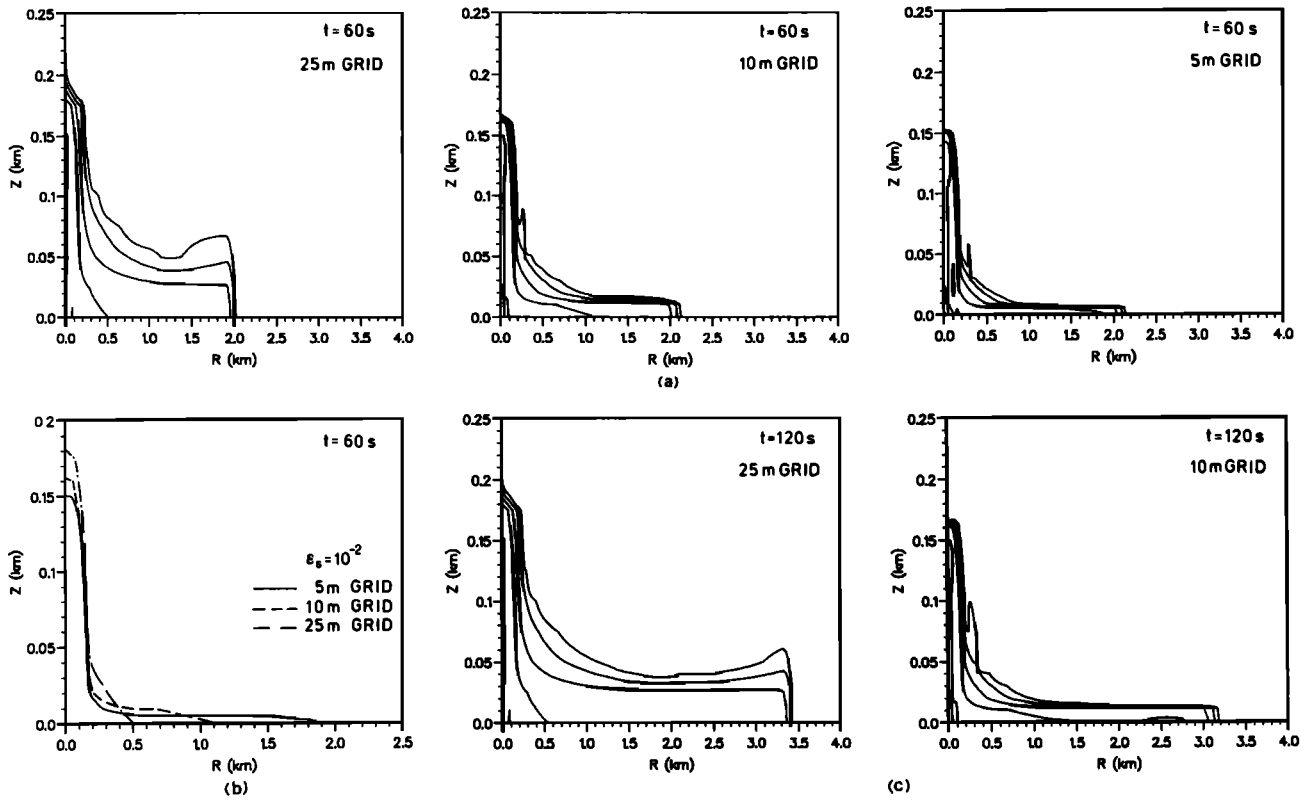

Fig. 12. Summary of a convergence study of eruption A. The results show the effect of computational domain cell size on the particle volumetric fraction distribution at 60 and 120 s. (*a*) Distribution at 60 s for grid sizes of 25, 10, and 5 m. (*b*) Variation of $\varepsilon_s = 10^{-2}$ with different grid sizes at 60 s. (*c*) Distribution at 120 s for grid sizes of 25 and 10 m. The contour levels shown in Figures 12*a* and 12*c* are the exponents to the base 10 and, beginning from the outer or distant from the vent region, correspond to −5, −4, −3, and −2.

sation above the fountain. Whether or not this result is fully realistic requires a further study involving larger computational domains, since the boundary conditions used in the model may contribute to nonphysical results when strong vortex motions and air cross the computational domain boundaries at later stages of the eruption. Figures 13 and 14 illustrate the particulate volumetric fraction and gas temperature distributions in the atmosphere at 30, 60, 180, 300, 600, and 1000 s. The generation of fountain at about 2000 m height, lateral spreading of the column and collapse, growth of water vapor and ash clouds above the fountain and pyroclastic flow, and merging of the clouds into one large volcanic plume can be readily appreciated from Figures 13 and 14. The temperature of the pyroclastic flow is maintained very high prior to the formation of the co-ignimbrite cloud on top of the flow, and the temperature of the merged clouds is quite high even at 1000 s (see Figure 14). The pyroclastic flow reaches a distance of 12 km at about 250 s, and at about 300 s the ash cloud above the fountain reaches a height of 20 km.

The results of convergence study with 100-, 50-, and 25-m uniform grids are shown in Figure 15 for the simulation times of 120 and 300 s. It is clear that a cell size decrease produces differences in the evolution of the pyroclastic flow head and thickness but no significant difference in the fountain height. Furthermore, the difference in the results between the 50- and 25-m cell sizes is minimal, and it appears that the latter cell size is adequate for the simulation of eruption B. The convergence study involving a cell size of 100 m, but with time steps of 0.1 and 0.2 s and domain sizes of L = 10–12 and H = 10–20 km, produced negligible differences in the results and are not reported in the paper. Employing the cell size of 25 m, the water vapor volumetric fraction distribution in the atmosphere at t = 30, 60, 120, 300, 420, and 540 s is illustrated in Figure 16.

The formation of the pyroclastic flow instabilities leading to the generation of the convective or co-ignimbrite-type clouds above the flows is clearly evident in Figures 13, 14, and 16, which involve computations on different grids. The 100-m cell size produces a rising cloud above the pyroclastic flow at about 6 km from the vent (Figure 13), whereas the 25-m cell size produces an instability at about 3 km from the vent. The latter instability develops at about 200 s and produces a rising cloud with entrained ash that subsequently (at about 420 s) joins the column above the fountain and entrains air into the column. The column collapse, formation of recirculating flows above the fountain, recirculation of ash into the column, and air entrainment above the pyroclastic flow are clearly visible in Figure 17 in a velocity vector plot.

The formation of the pyroclastic flow instability leading to the generation of a convective or co-ignimbrite-type cloud above the flow is depicted in Figure 18 at 180 and 300 s. Figure 18 shows the vertical distributions of mixture density, gas density, and gas temperature at radial positions in the pyroclastic flow that contain the unstable convection region. At 180 s (Figure 18*a*) the water vapor is mainly contained in the pyroclastic flow and the two-phase or mixture density is larger than the air density (except in a thin layer) above the

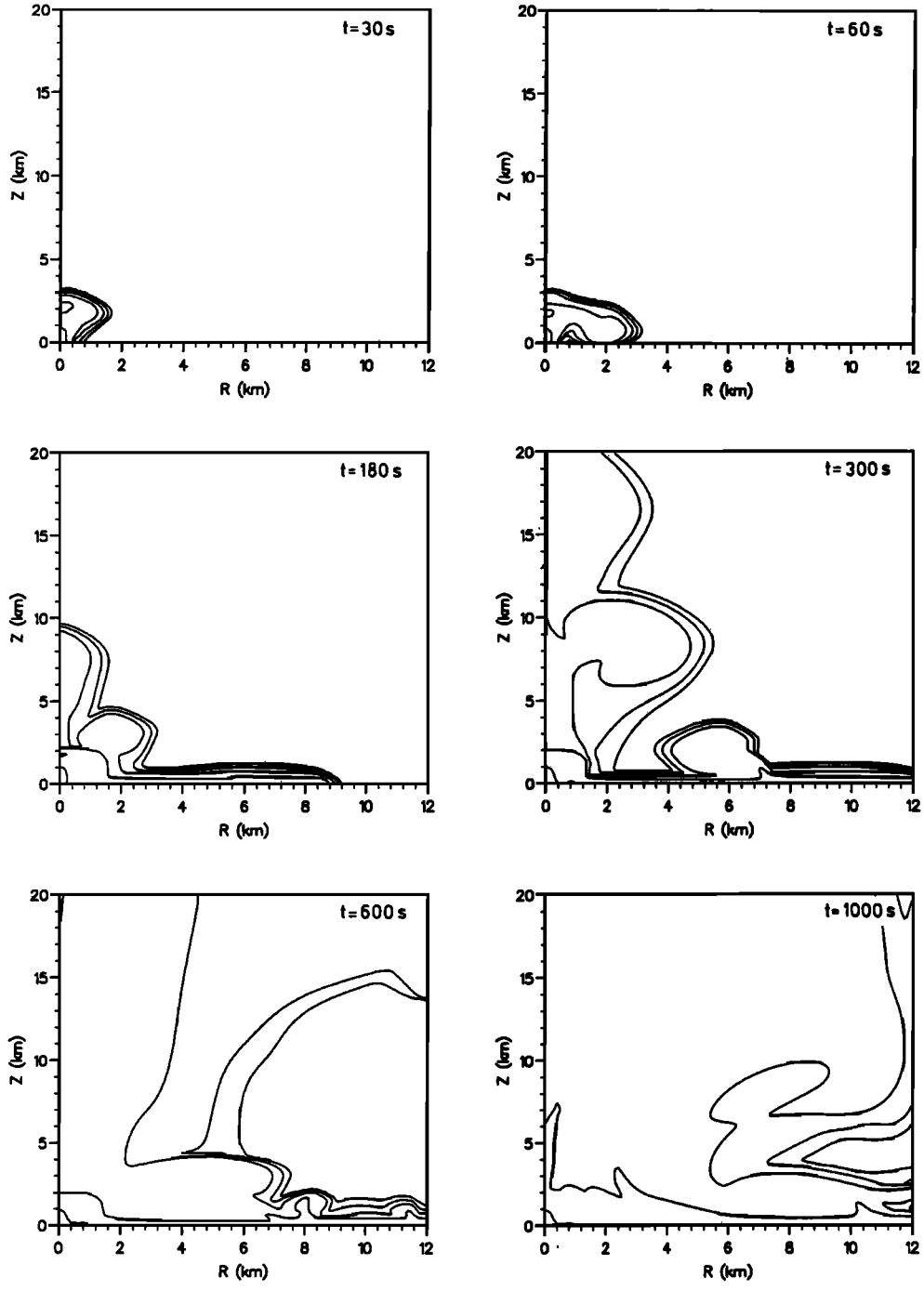

Fig. 13. Distribution of the particulate volumetric fraction in the atmosphere of eruption B at 30, 60, 180, 300, 600, and 1000 s for a cell size of 100 m. The building of a fountain at about 2000 m height, lateral spreading and collapse of column, and the development of pyroclastic flow and ash clouds above the fountain and pyroclastic flow are readily apparent. The contour levels shown are the exponents to the base 10 and correspond to −10, −8, −6, −4, and −2, starting from the outer contour or far from the vent region.

flow. At 300 s, however, the mixture density close to the impermeable wall has increased considerably due to the particulate sedimentation (Figure 18*b*), whereas in the upper layers of the pyroclastic flow it has decreased. At this time the convective instability above the flow has already settled in and a phoenix cloud is developing rapidly. The conditions leading to the formation of this buoyant cloud above the pyroclastic flow are similar to the conditions which produce a cloud above the collapsing column. The latter plume is formed earlier because of the more favorable conditions for convective instability which exist during the column collapse stage. It should be noted that eruption A also develops a cloud above the fountain and the collapsing column but apparently with a less efficiency than do eruptions B and C, which contain a larger quantity of water.

The distribution of fountain heights and maximum pres-

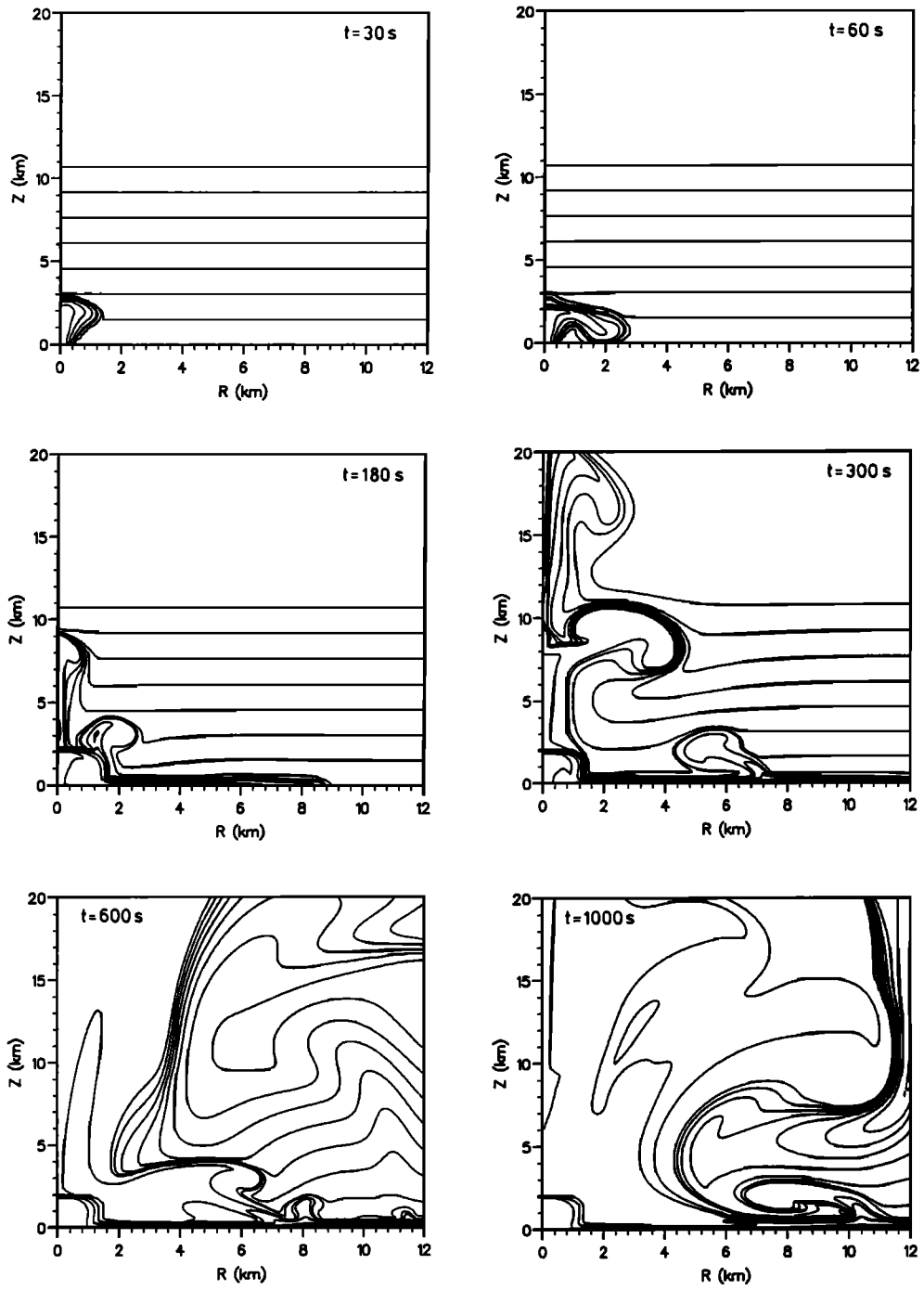

Fig. 14. Gas temperature distribution in the atmosphere of eruption B with a cell size of 100 m at 30, 60, 180, 300, 600, and 1000 s. Note the high temperature that is maintained by the pyroclastic flow before water vapor starts separating and building a cloud. The high water vapor content in the atmosphere at 1000 s is reflected in high temperatures of gas over a very large region. A contour level represents the difference between the local gas temperature and the undisturbed atmospheric air temperature at $Z = 0$. The temperature contours, starting from the inner contour or near the vent region, correspond to 900, 800, 500, 200, 100, 0, −10, −20, −30, −40, −50, −60, and −70 K.

sure and density in the column with time is shown in Figure 19. Figure 19*a* shows the fountain heights corresponding to the maximum pressure near the top of the fountain and the pressure equal to atmospheric, whereas Figure 19*b* illustrates fountain heights corresponding to the maximum mixture density in the fountain and the density equal to atmospheric. The maximum in pressure and density in the fountain is reached several seconds later than the maximum height of the fountain, for the same reason as discussed above for eruption A. The fountain heights and maximum pressure and density show an oscillatory behavior which is not evident for eruption A. These oscillations can be assumed to arise from the physics of the gas and particle recirculation from the collapsed column into the fountain

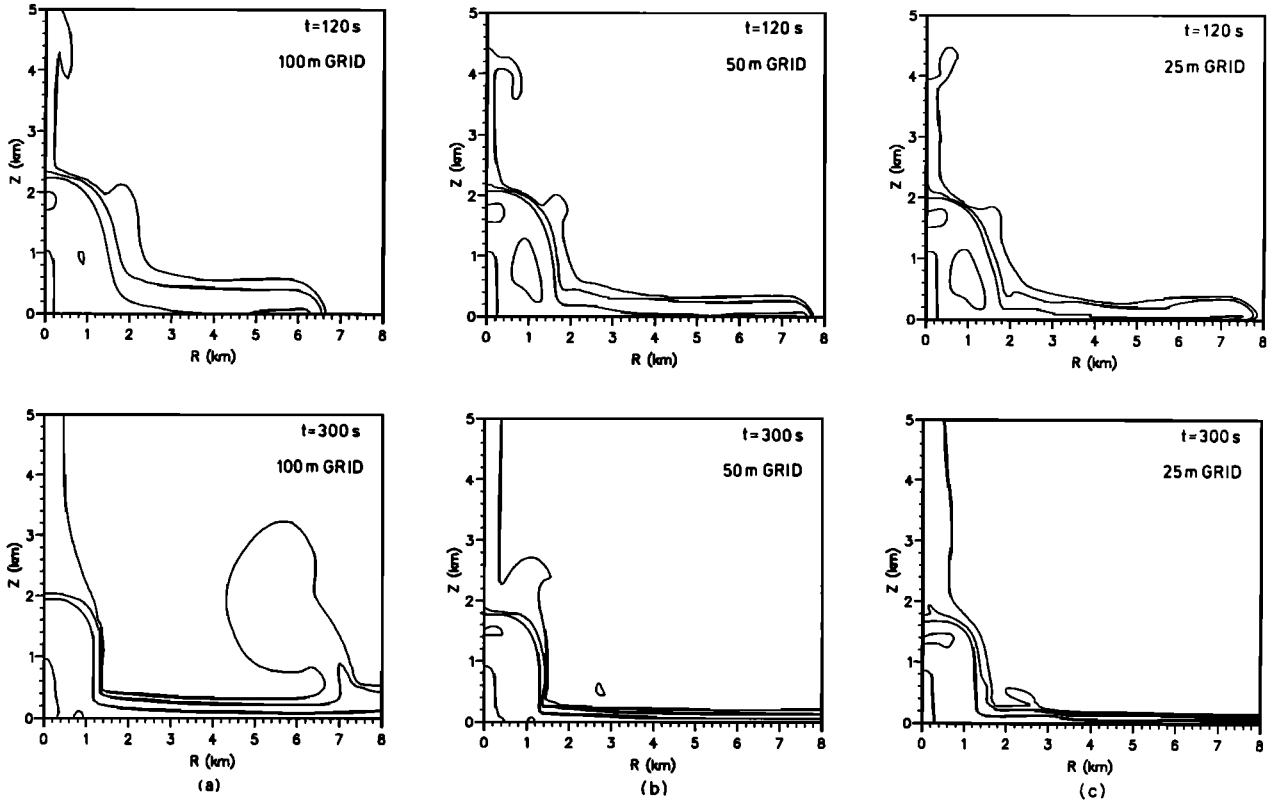

Fig. 15. Distribution of the particulate volumetric fraction at 120 and 300 s of eruption B employing a cell size of (*a*) 100 m, (*b*) 50 m, and (*c*) 25 m. The contour levels shown are the exponents to the base 10 and, beginning from the outer contour or far from the vent region, correspond to −5, −4, −3, and −2.

and have a period of about 40 s. Referring to Figure 19*c*, it may be seen that an average travel distance of gas and particles during a recirculation time is about four fountain heights, which translates into an approximate time of travel of

$$T_{cycle} \approx \frac{4Z_c}{v_v} = \frac{2v_v}{g} \approx 40s \qquad (44)$$

where use was made of (37). A comparison between this result and numerically predicted value of the oscillation period appears to justify the above assumption. The amplitude of fountain height oscillation in Figures 19*a* and 19*b* is about 200 m. By using (44) the oscillation period of eruption A should be about 11 s, but the results from numerical simulations do not confirm this, even with a computational grid size of 5 m. It may be concluded therefore that eruption B is more underdamped than is eruption A. The column collapse height of eruption B is about 1700 m (Figures 19*a* and 19*b*), and it compares favorably with a value of 2050 m as obtained from (37). In their work on collapsing volcanic columns, *Valentine et al.* [1991] discuss oscillations of the ash mass flux at fixed vertical locations above the vent and associate these oscillations with the material recycling of the collapsed column into the fountain with the periods which are larger than ours (about 130 s). This difference in periods between their and our simulations can be associated with different vent geometries and two-phase flow conditions. We are currently involved in a more detailed study of the parameters affecting the collapsing column behavior in order to understand the physics of column oscillations.

The normal Mach number distribution for this eruption is similar to that of eruption A as shown in Figure 9, except that the weak shock angle δ is found to be about 40°. A strong recirculation of the pyroclastic flow material into the jet and fountain produces, however, a much more complicated rotational flow structure above and near the vent than in eruption A and is attested by the complicated Mach reflections of this column.

Eruption C

The eruption C has the same vent diameter, particle characteristics, and exit pressure as eruption B, except that the exit flow velocity is 250 m/s and the particle volumetric fraction is 0.005. Since this eruption contains more water vapor than eruption B, its collapse height is about 3800 m, and it produces a thick pyroclastic flow. This eruption was simulated with (1) 100-m uniform grid, L = 12 km, and H = 20 km and (2) 50-m uniform grid, L = 6 km, and H = 10 km.

The development of fountain, column collapse, pyroclastic flow and column above it, and merging of clouds above the fountain and pyroclastic flow is shown in Figure 20 for the 100-m grid size in order to illustrate the large-scale behavior of the column. After 60 s, when the column has built a fountain, the radial momentum loss at the top of the column leads to the column collapse. At 120 s the column has already hit the ground, and two radial motions of the

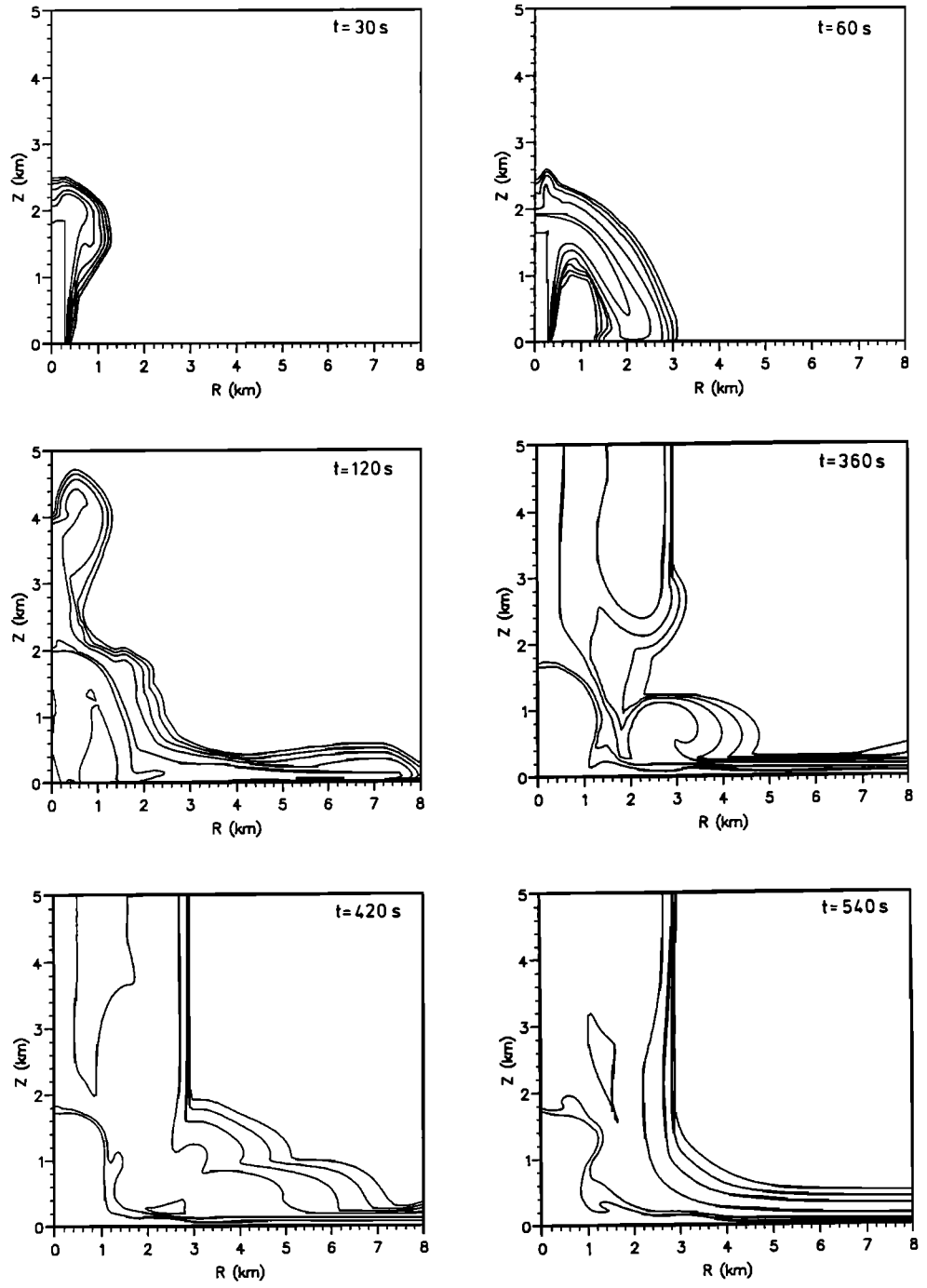

Fig. 16. Distribution of the water vapor volumetric fraction in the atmosphere of eruption B at 30, 60, 120, 360, 420, and 540 s. The cell size used in the computations corresponds to 25 m. The contour levels shown are the exponents to the base 10 and, starting from the outer contour or far from the vent region, correspond to −10, −8, −6, −4, −2, −1, and 0.

gas-particle mixture are noticed, one radially outward which forms the pyroclastic flow and the other radially inward. The inward motion of gas and particles heats the trapped air below the collapsed column and produces particle sedimentation close to the vent and mixture density decrease in the collapsing column. This density decreases produces a large buoyancy effect and leads to the formation of two unstable regions, one on top of the collapsing column at about 180 s and 2 km from the vent, and the other at about 240 s at 4 km from the vent (not shown in Figure 20). By 360 s the convective instabilities produce large clouds which begin to merge and neck inward at subsequent times. The large necking effect which is visible at 470 s is produced from a very intensive upward convective motion which must decrease the flow area in order to maintain the conservation of mass. At 470 s the pyroclastic flow becomes unstable at larger distances from the vent. The simulation was not carried out beyond this time due to the water vapor conden-

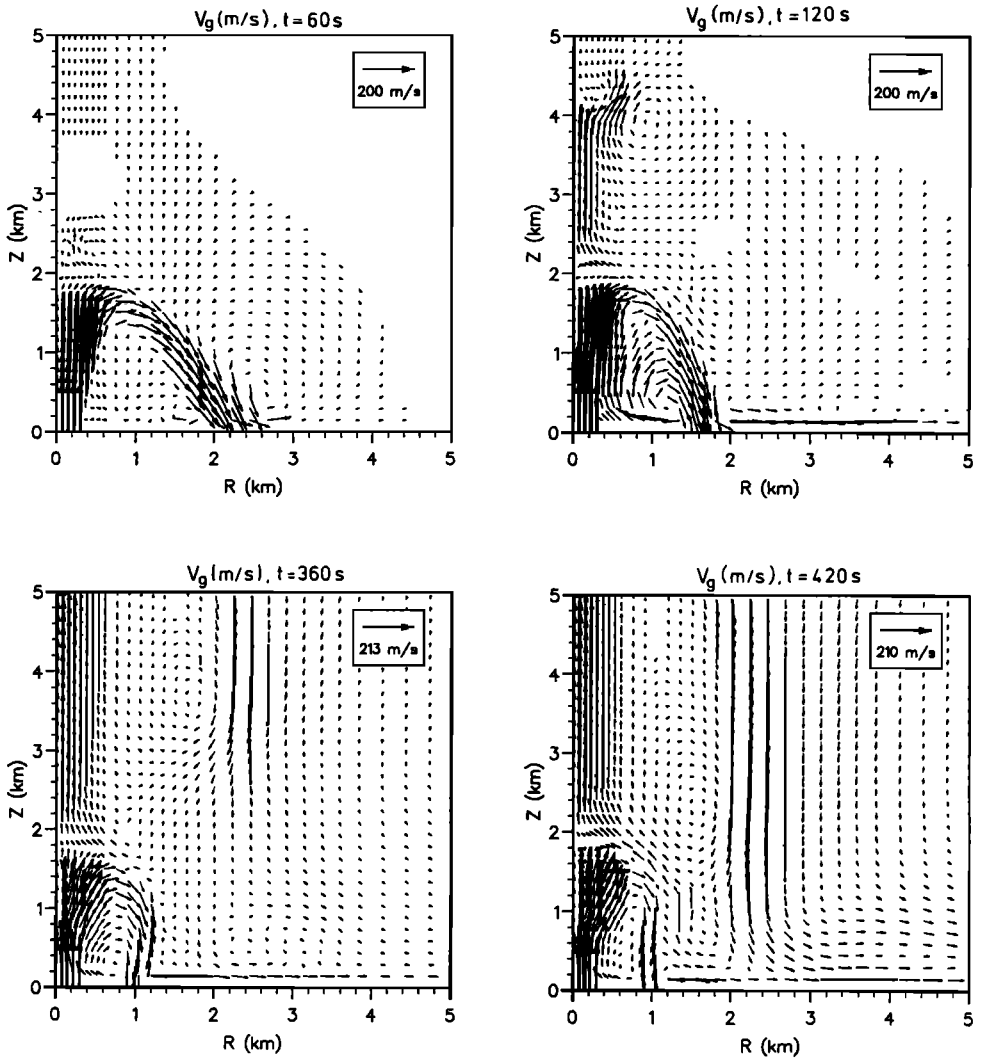

Fig. 17. Gas velocity vector plots of eruption B with a cell size of 25 m at 60, 120, 360, and 420 s. Notice the recirculating flows below the collapsed column and above the fountain and pyroclastic flow. These velocity plots do not show velocities that are 100 times less than the maximum velocities which are reported in the inserts.

sation on top of the fountain, but it appears that the flow develops more phoenix clouds at later times.

Figure 21 shows a comparison between the particle volumetric fraction distributions performed with the 100 and 50 m cell sizes at 60, 120, and 180 s. As shown in Figure 21 the 50-m cell size results are noticably different from the 100-m cell size and confirms the previous conclusions that each column should be simulated with different computational parameters before accepting these results. The fountain heights corresponding to the maximum and atmospheric pressure and density in the column at the symmetry axis are illustrated in Figure 22. During the early transient period when the column builds a fountain, its pressure and density distributions are similar as for eruptions A and B (see Figures 8 and 19). (The minimum in P_{max} in Figure 22 is caused by the decrease of the atmospheric pressure with height.) The oscillations of the fountain at later times, which are not as well defined as for eruption B, may be associated with different inertial and damping characteristics of this column. The column collapse height of eruption C using (37) is about 3185 m and compares favorably with the numerical prediction of about 3400 m. Such an underestimation of the fountain height can be associated with a low column density (or a large column buoyancy) which is not properly modeled by (37).

Discussion

The general conclusions from the simulations of collapsing volcanic columns presented here are consistent with those of *Valentine and Wohletz* [1989*a*], *Wohletz and Valentine* [1990, 1991], and *Valentine et al.* [1991, 1992]. These conclusions confirm previous results that the transient behavior of gas-particle mixtures can last for several minutes above the vent even with a steady discharge from the vent. The results from the present numerical simulations show the importance of including the water vapor into modeling which promotes convective instabilities and the granular flow model which should model the column dynamics and pyroclastic flows better than in the past. The unsteadiness in temperature, velocity of gas and pyroclasts, pyroclasts volumetric fraction, etc. can be associated not only with the recirculation of pyroclastic flow material into the base of the column and ash entrainment from the top of the pyroclastic flow by atmospheric inflow back toward the column but also

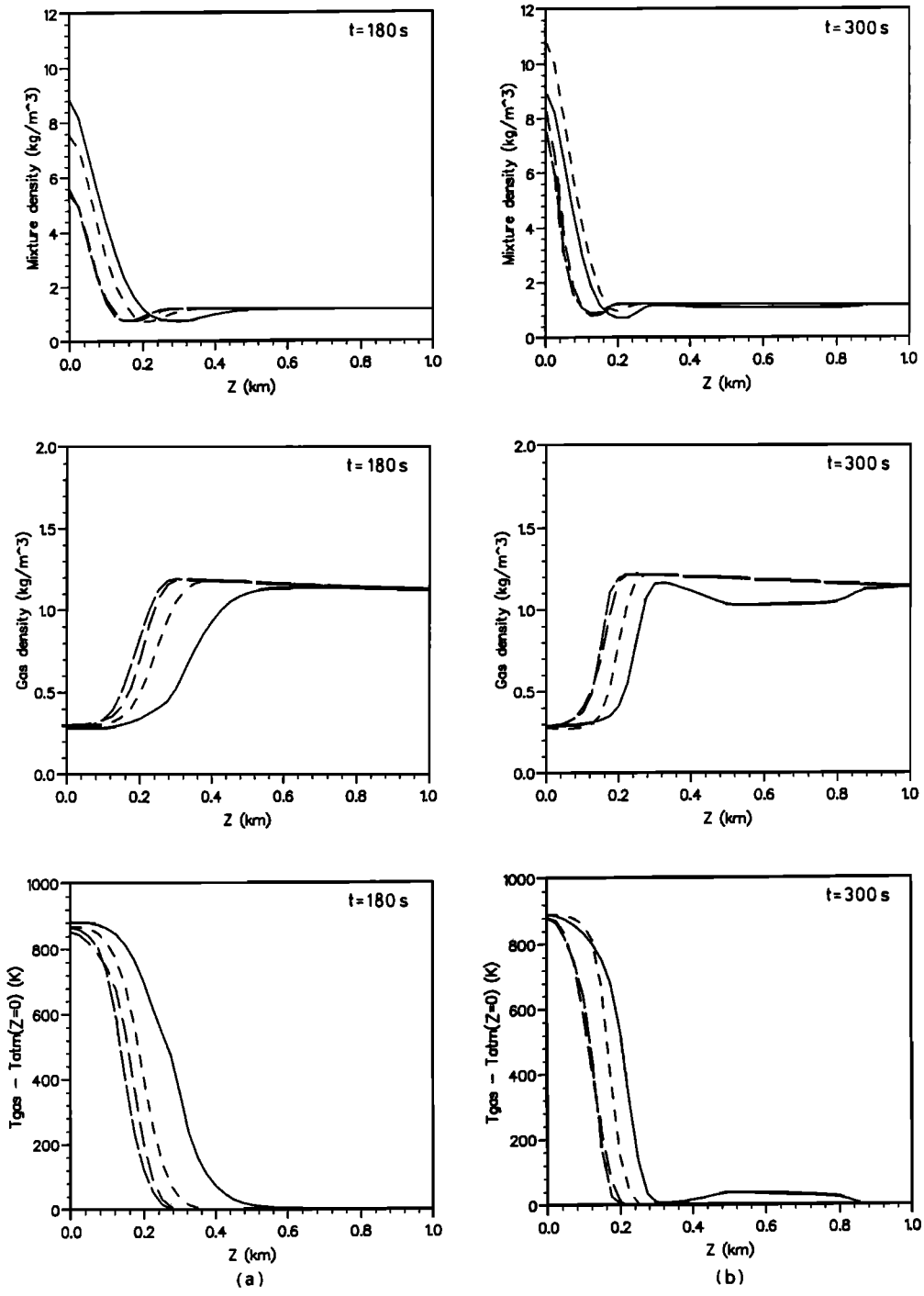

Fig. 18. Vertical distributions of mixture density, gas density, and gas temperature at radial positions (*a*) 180 s and (*b*) 300 s in the pyroclastic flow of eruption B with a cell size of 25 m. The flow contains an unstable region which produces a rising column above the flow. The curves in the figure correspond to R = 2 km (solid line), R = 3 km (short-dashed line), R = 4 km (medium-dashed line), and R = 5 km (long-dashed line).

with water vapor mixing with a denser atmosphere which can produce unstable density gradients and promote convective instabilities. The complex thermo-fluid dynamic processes in the column can be responsible for the creation of complex compositional gradients of pyroclastic material near and far from the vent, and it may be dangerous to interpret these gradients solely on the basis of compositional gradients arising within a magma chamber.

The numerical simulations reproduce the experimental observations of *Carey et al.* [1988] whereby the high particle concentration eruptions develop fountains, radially spreading pyroclastic flows, sedimentation of particles in the flow and resulting flow instabilities which produce rising columns on top of the flows, and merging and necking of the co-ignimbrite clouds with the main clouds above the fountains into large volcanic plumes.

The co-ignimbrite columns developed during the eruptions of Tambora (1815) [*Sigurdsson and Carey*, 1989], Krakatau

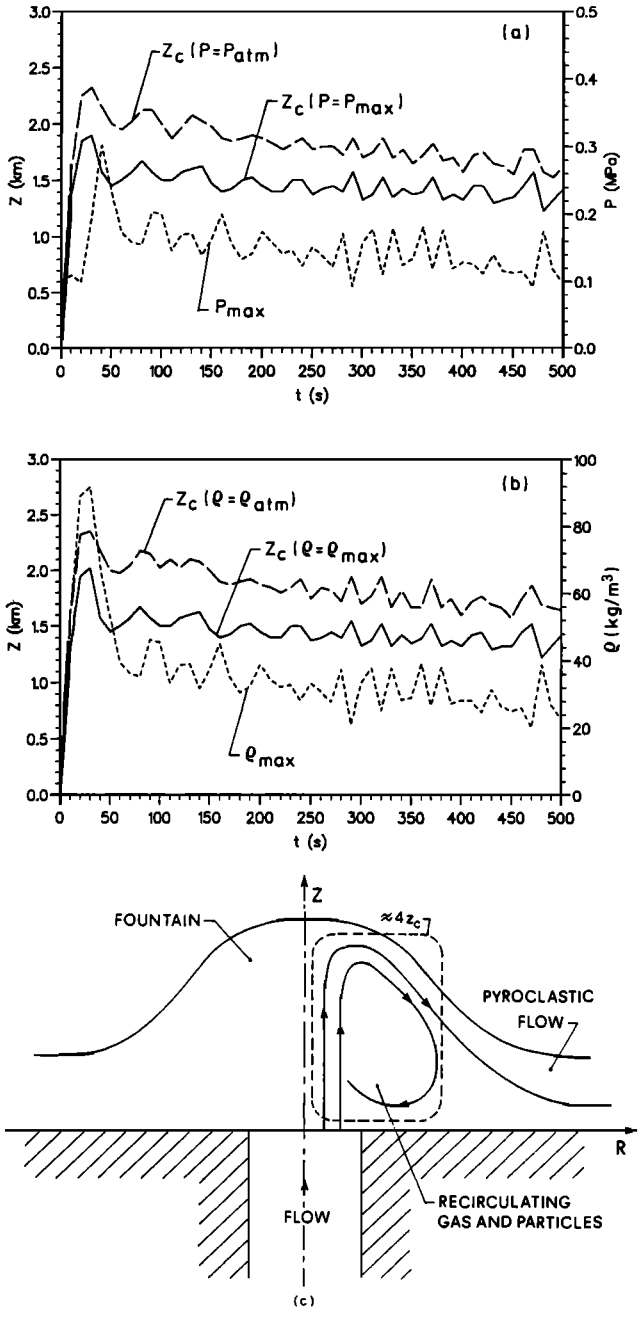

Fig. 19. Timewise distributions of fountain heights and maximum pressure and density in the column of eruption B with a cell size of 25 m. (*a*) Fountain heights corresponding to the maximum pressure near the fountain top and the pressure corresponding to atmospheric, all along the symmetry axis. The quasi steady state heights correspond to about 1800 and 1500 m. (*b*) Similar distributions of mean density and the associated heights in the fountain. These quasi steady state heights correspond to about 1800 and 1500 m. (*c*) Sketch showing an approximate distance traveled by a gas or solid particle during a recycling period.

(1883) [*Self and Rampino*, 1981], Santorini [*Sparks and Huang*, 1980], Toba in Sumatra (75,000 years B.P.) [*Rose and Chesner*, 1987; *Rampino and Self*, 1992], etc. The estimated mass eruption rates of these eruptions are of the order of 10^9 kg/s with column heights reaching 30–40 km [*Woods and Wohletz*, 1991]. The eruptions B and C discussed above clearly belong to the very large scale volcanic events, but we did not establish from limited simulation times how high the clouds rise. For this purpose, one must perform simulations with very large computational domains and a large number of cells to adequately resolve the important gradients in the fountain and pyroclastic flow. The July 22 and August 7, 1980, eruptions of Mount Saint Helens formed fountains, pyroclastic flows, and ash clouds above the flow [*Hoblitt*, 1986]. A fountain of July 22 reached a height of 800 m, and the ash clouds above the pyroclastic flow rose more than 4000 m. *Sparks and Wilson* [1976] and *Sparks et al.* [1978] argue that the columns produce fountains because the gas thrust phase of the eruption cannot produce sufficient heating of air to reduce its mean density below the undisturbed air density at the height where the upward velocity is reduced to zero. The presented numerical results generally confirm this conclusion. A fountain height depends on the conditions of the gas and pyroclasts at the vent. As Figures 7, 8, and 19 show, the fountain height initially increases to a large value before leveling off to a quasi steady state or an oscillatory behavior. These oscillations require a further study, but it appears that they are associated with the period of material recycling into the fountain and damping characteristics of the system. The results from simulations also show that with simulation periods of several minutes no convection recovery or destruction of fountains takes place once they are formed. For this to take place, it appears that a change in the vent conditions or a perturbation of the two-dimensional flow field above the vent is required. It should also be noted that the vent conditions in Table 2 producing collapsing fountains are consistent with plume theory predictions [*Wilson and Walker*, 1987; *Woods*, 1988; *Bursik and Woods*, 1991].

The numerical predictions of the speeds of propagation of pyroclastic flows are different on the upstream and downstream sides of the location of co-ignimbrite clouds. The results of eruption A show that the maximum horizontal speed of 40 m/s occurs at about 200 m from the vent and that it is reduced to about 20 m/s just before the pyroclastic flow instability and to 5 m/s after the phoenix cloud has formed above the pyroclastic flow (see Figure 11). Immediately after the column hits the ground, the speed of propagation of pyroclastic flow of column B (with a grid size of 25 m) is about 100 m/s, whereas that of column C (with a grid size of 50 m) is about 60 m/s. These speeds represent average values and do not change significantly after the onset of pyroclastic flow instabilities, probably due to the small particle size used in the simulations which produce low sedimentation rates. The above results on the speeds of propagation of pyroclastic flows can be compared with the results of a simple collapsing column modeling of *Wilson* [1976] and *Sparks et al.* [1978], which predict the speeds of propagation of pyroclastic flows of 130 m/s for column B and 150 m/s for column C. This discrepancy is attested by the crude modeling of the buoyancy effects in the simple model which becomes especially relevant for eruption C. The pyroclastic flow speed during the first eruption of Mount Saint Helens on July 22, 1980, was estimated to be 40 m/s on a 10° slope at 1.2 km from the vent prior to the formation of the co-ignimbrite cloud [*Hoblitt*, 1986] which is comparable with the speed of propagation of pyroclastic flow of eruption A with a 0° slope.

The column collapse height computed by the model of *Wilson* [*Wilson*, 1976; *Sparks et al.*, 1978] gives about 200 m for eruption A, 1700 m for eruption B, and 2000 m for

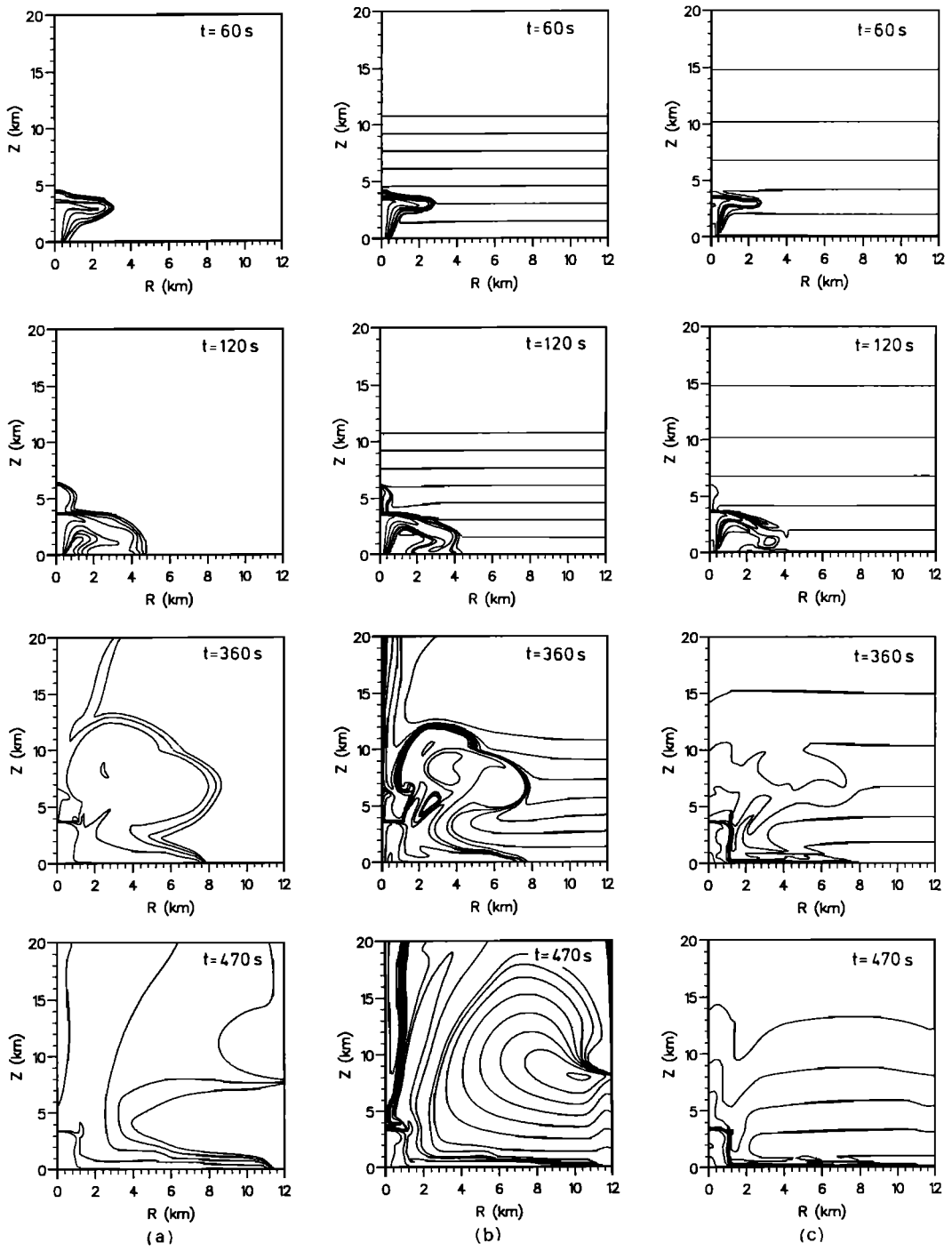

Fig. 20. Development of eruption C at 60, 120, 360, and 470 s using a cell size of 100 m. (*a*) Particle volumetric fraction distribution. (*b*) Gas temperature distribution. (*c*) Two-phase flow mixture density distribution. The figures show the development of a fountain at about 60 s, collapse of the column, rising clouds from the collapsing column, and development of more clouds above the pyroclastic flow at late times. The particle fraction contours shown are the exponents to the base 10 and, starting from the outer contour or far from the vent region, correspond to −10, −8, −6, −4, and −3. The temperature contours represent the difference between the gas temperature and the temperature of the undisturbed atmosphere at $Z = 0$. Starting from the inner contour or close to the vent region, the temperature contours correspond to 900, 800, 500, 200, 100, 0, −10, −20, −30, −40, −50, −60, and −70 K. The mixture density contours, starting from the inner region, correspond to 10, 5, 2, 1.2, 1, 0.8, 0.6, 0.4, and 0.2 kg/m^3.

eruption C. Comparing these results with the numerical predictions summarized in Table 2 shows a considerable disagreement for large-scale eruptions where buoyancy effects near the vent play a large role in the establishment of a steady state fountain height. A simple pyroclastic flow modeling approach that ignores the segregation of particles from gas and the mixing of the hot water vapor and air from the top layers of the pyroclastic flow with cold air layers above the flow cannot predict the important pyroclastic flow phenomena associated with flow instability that produces a

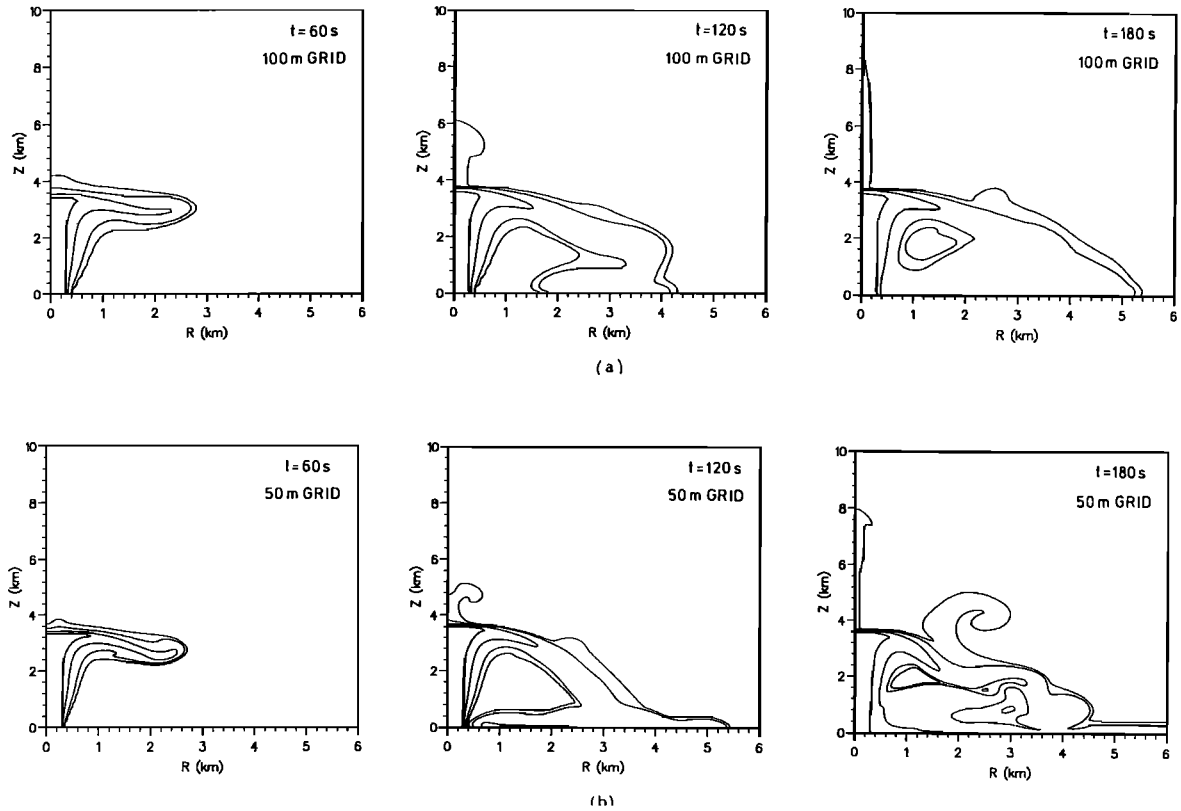

Fig. 21. Distribution of the particulate volumetric fraction at 60, 120, and 180 s of eruption C employing a cell size of (*a*) 100 m and (*b*) 50 m. The contour levels shown are the exponents to the base 10 and, beginning from the outer contour or far from the vent region, correspond to −5, −4, −3, and −2.5.

rising cloud above the flow and changes in the thermo-fluid dynamics in the flow in front of the cloud. This is especially relevant for the large-scale eruptions where large spatial extents can lead to an early development of co-ignimbrite clouds after the columns develop fountains several kilometers high.

The emplacement temperatures of pyroclastic flows determine the degree of welding, compaction, recrystallization, and chemical alteration [*Smith*, 1960; *Sparks et al.*, 1978]. Very thick and voluminous ignimbrites can be completely nonwelded, whereas thin ignimbrites can be densely welded throughout much of their thickness. The pyroclastic flow emplacement temperature depends on both the vent conditions and degree of convective mixing in the atmosphere. The pyroclastic flow temperatures of eruption A vary from about 1100 K at $Z = 0$, 800 K at $Z = 10$ m, and 400 K at $Z = 20$ m above the ground or the outer edge of the flow (Figures 10 and 11); eruption B exhibits variations from 1100 K at $Z = 0$, about 900 K at $Z = 150$ m, and about 400 K at $Z = 200$ m height at the outer edge of pyroclastic flow (Figure 18); eruption C exhibits variations from 900 K at $Z = 0$, about 800 K at $Z = 250$ m, and about 400 K at $Z = 500$ m at the outer edge of the flow (Figure 20). These results demonstrate that the pyroclastic flow has a greater temperature and cools more slowly with a decreasing quantity of water vapor exiting from the vent because of the smaller mass of water vapor that is involved in the exchange of heat with the cold air. The emplacement temperature of dacite and ash pumice of the July 22, 1980, eruption of Mount Saint Helens is estimated at 900 K, where the greatest lateral emplacement temperature gradient was observed near the vent [*Hoblitt*, 1986]. Such a cooling effect near the vent is fully confirmed by the presented results.

Ignimbrites typically contain a wide range of particle sizes, ranging from few microns to as much as a meter [*Sparks and Wilson*, 1976]. The larger particles sediment first, whereas the small particles of few microns follow the turbulent fluctuations of the gas phase and can be transported with gas to large distances. In the numerical simulations use was made of uniform size particles ranging from 200 μm for eruption A and 10 μm for eruptions B and C. As such, eruption A yields higher particle sedimentation rates and larger velocity and temperature nonequilibrium between the phases than do eruptions B and C. This nonequilibrium is small, however, and for this reason the particle temperature, which is essentially equal to the gas temperature, was not discussed. The most significant velocity differences (several meters per second) between the phases occur above the vent, when the column collapses and hits the ground, below the co-ignimbrite cloud, and in the head of the pyroclastic flow. The above results are also consistent with the granulometric studies of pyroclastic flow deposits, which show that particles which are smaller than few tens of microns are not preferentially deposited along the flow as opposed to the large size particles which segregate from the flow and give rise to a coarse-tail grading [*Cas and Wright*, 1987]. In addition, volcanological observations and field data [*Wilson and Walker*, 1982; *Wilson*, 1985; *Cas and Wright*, 1987] suggest that pyroclastic flows terminate where the co-

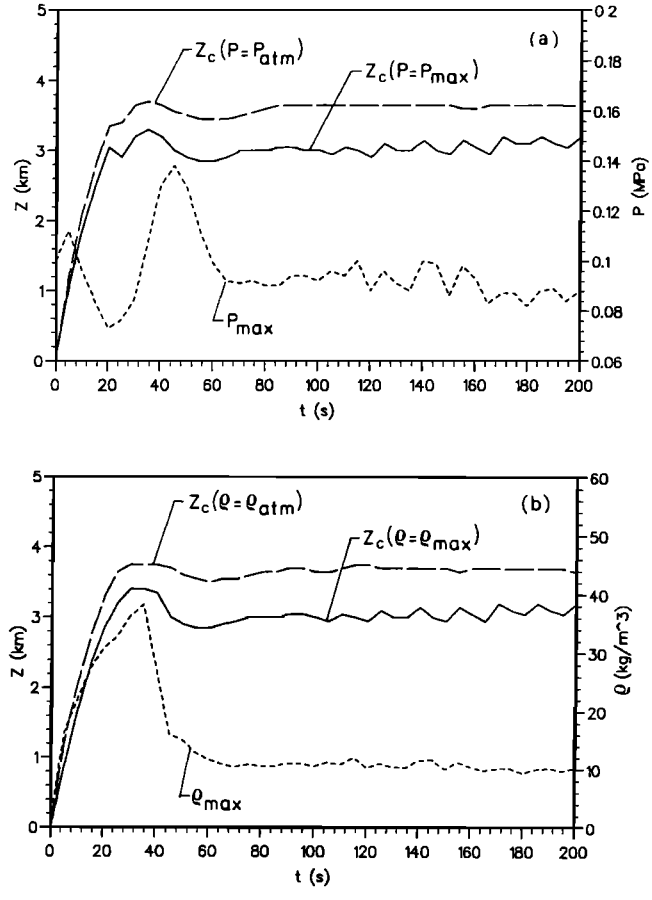

Fig. 22. Timewise distributions of fountain heights and maximum pressure and density in the fountain of eruption C. (*a*) Fountain heights corresponding to the maximum pressure near the fountain top and the pressure corresponding to atmospheric, all along the symmetry axis. (*b*) Similar distributions of mean density and the associated heights in the fountain.

ignimbrite columns form, which is in accord with our results of eruption A which involves particles of large size.

Real pyroclastic flows appear to consist of a basal avalanche that underlies an ash cloud. The basal avalanche appears to consist of a highly concentrated dispersion of blocks, lapilli, and ash whose collisions produce a layer of saltating particles below the ash cloud [*Denlinger*, 1987]. A rigorous modeling of a pyroclastic flow may require the consideration of a number of particle size classes or phases with particle fragmentation taking place. In our present model only one particle size class was employed, and therefore it may be dangerous to extrapolate the detailed behavior of pyroclastic flows from present simulations to the real pyroclastic flows.

Because of a low collapsing height, eruption A required a very small grid size to resolve adequately the flow gradients. The 10-m grid size in the proximity of the impermeable boundary and in the fountain appears to be adequate, although some computations with a 5-m grid show that the pyroclastic flow thickness has not yet achieved a converged value for small particle volumetric fractions (Figure 12). The 5-m grid size computations with radial and vertical extents of several kilometers may require in excess of a million grid points, which is beyond the present simulation capabilities. Eruptions B and C produce thick pyroclastic flows, and it appears that a 50-m grid is adequate (see Figures 15 and 21) to resolve the important properties of these columns. A 25-m grid size is better, but it may then require over 500,000 grid points to simulate an eruption with radial and vertical extents of 20 km. This number of grid points is too large, however, for simulating a column with present computational tools.

The convergence studies have demonstrated a need for carefully evaluating each volcanic simulation for the effect of computational parameters on the results.

SUMMARY AND CONCLUSIONS

A complex thermo-fluid dynamic two-phase and two-component flow model was implemented to simulate collapsing volcanic columns. The model involves only one particle size class and accounts for water vapor mixing with air in the atmosphere. The effect of particle collisions in the model was accounted by a kinetic theory model that solves for the granular temperature and therefore predicts the particle viscosity and pressure. The effect of gas phase turbulence was accounted by a turbulent subgrid scale model, but the effect of particles on the gas turbulence modulation was not. The partial differential equations involving the conservation of mass, linear momentum, energy, and granular temperature were numerically solved for an axisymmetric flow configuration with different geometries and two-phase flow conditions at the vent. The numerical solutions involved different grid sizes and computational domains in order to assess the effects of these parameters on the results.

The simulated volcanic eruptions produce fountains at about 150 m, 1700 m, and 3400 m height. Each of these eruptions produces a radially spreading flow above the vent before the eruption column loses its radial momentum and begins collapsing. The collapsed column builds an outward spreading pyroclastic flow and an inward flow of material which is recirculated into the jet and fountain. The jet thrusting into the atmosphere produces an inward flow toward the axis and builds compression waves which subsequently reflect from the symmetry axis as Mach waves and form a complex flow pattern in the upper regions of the fountain due to the viscous effects. After an initial transient period lasting from tens of seconds to several minutes, each fountain develops a steady state or an oscillatory fountain height. The fountain height oscillations appear to be connected with transit times of gas and particle recirculation into the column which depend on the grid size employed in the numerical solution and on the relative importance of inertial and damping forces of the flow. For large grids these oscillations are suppressed, and the fountain develops a steady state height. Two different definitions of fountain height are possible, one corresponding to the vertical location where the gas-particle mixture density and pressure are reduced to the undisturbed density and pressure of local atmosphere and the other corresponding to the maximum density and pressure near the top of the fountain; both are defined along the axis of symmetry.

After the radially spreading pyroclastic flow begins to loose momentum and starts sedimenting particles, it becomes unstable due to the mixture density decrease. This density decrease produces unstable convection or phoenix clouds of water vapor, air, and particles above the pyroclas-

tic flow. When the pyroclastic flow builds a phoenix cloud, its radial spreading rate diminishes considerably. The pyroclastic flow temperature is very high, and a larger flow cooling rate is associated with a larger quantity of water vapor erupting from a vent. The vertically rising cloud from a pyroclastic flow necks and joins the cloud above the fountain to form a large volcanic plume. In large volcanic eruptions it is possible for top layers of a collapsing column to become unstable before and after the development of pyroclastic flow. This effect in large eruptions with large fountain heights can be associated with large cooling regions where the convective instabilities develop early and create spawning clouds.

The numerical simulations of several collapsing volcanic columns with grid sizes from 5 to 100 m and computational domains up to 12 km wide and 20 km high demanded large computer resources. To surmount the computational difficulties and adequately resolve the physics, small grid sizes in the regions of high flow gradients were employed. The numerical modeling of collapsing volcanic columns is especially difficult since they produce different structural features in different regions of the flow, and because they can generate very large volcanic plumes that may rise high into the atmosphere. An accurate modeling of local column phenomena is therefore of considerable importance, since these phenomena can be responsible for global column behavior. The success in future detailed modeling of the pyroclastic-flow-generating volcanic columns will depend on the resolution of the fine structural details in the flow by modeling a polydispersed mixture of gases and particles with and without topographic barriers.

The results from simulations were shown to be consistent with simple column modeling approaches, laboratory experiments, and field observations. This consistency is, however, only qualitative, and a great need exists to produce the volcanic column field data that can be used to verify the results from detailed physical modeling of the columns. Only with such a verification may be possible in the future to construct real volcanic simulators [*Dobran et al.*, 1990; *Dobran and Mulargia*, 1991].

NOTATION

a speed of sound in the gas-particle mixture.
C_d drag coefficient.
Cp specific heat at constant pressure.
d particle diameter.
D interfacial drag.
D_v vent diameter.
e restitution coefficient.
$\mathbf{g}$ gravitational body force per unit mass.
g_0 radial distribution function.
h enthalpy.
H vertical extent of the computational domain.
$\mathbf{I}$ unit tensor.
k thermal conductivity.
L radial extent of the computational domain.
$\dot{m}$ mass flow rate.
M molecular weight.
$\mathbf{M}$ Mach number.
M_n normal Mach number.
Nu Nusselt number.
P pressure.
Q volumetric heat transfer rate.
R radial coordinate.
$\bar{R}$ gas constant.
$\mathcal{R}$ universal gas constant.
Re Reynolds number.
t time.
T temperature.
T_K granular temperature.
$\mathbf{T}$ stress tensor.
u radial component of velocity.
v vertical component of velocity.
$\mathbf{v}$ velocity vector.
x mole fraction of a component in the gas phase.
y mass fraction of a component in the gas phase.
Y mass fraction of gas phase in two-phase mixture.
Z vertical coordinate.

Greek

γ collisional energy dissipation.
δ weak shock turning angle.
ε volumetric fraction of gas or solids.
θ azimuthal angle.
κ fluctuating energy conductivity.
λ_s slip parameter.
μ viscosity.
ξ solids or particles bulk viscosity.
ρ density.
τ viscous stress tensor.

Subscripts

a air.
c collapse.
g gas phase.
ge gas effective.
gt gasturbulent.
m mean or mixture.
min minimum.
M maximum.
s solids or pyroclasts phase.
v vent.
w water vapor.

Acknowledgments. This work was partially supported by the Gruppo Nazionale per la Vulcanologia, Italy. We also thank Franco Barberi for supporting the volcanological modeling approach, and Paolo Papale for useful discussions involving the volcanological issues. One of us (F.D.) gratefully acknowledges the hospitality and exclusive computer time offered by F. Informatica/ETSI Telecomunicacion of the Universidad de Malaga during the initial time of this work.

REFERENCES

Bursik, M. I., and A. W. Woods, Buoyant, superbuoyant and collapsing eruption columns, *J. Volcanol. Geotherm. Res.*, *45*, 347–350, 1991.

Carey, S. N., H. Sigurdsson, and R. S. J. Sparks, Experimental studies of particle-laden plumes, *J. Geophys. Res.*, *93*, 15,314–15,328, 1988.

Cas, R. A. F., and J. V. Wright, *Volcanic Successions*, Allen and Unwin, Winchester, Mass., 1987.

Chapman, S., and T. G. Cowling, *The Mathematical Theory of Non-Uniform Gases*, Cambridge University Press, New York, 1970.

Chepil, W. S., and N. P. Woodruff, Sedimentation characteristics of

dust storms, II, Visibility and dust concentration, *Am. J. Sci.*, *255*, 104–114, 1957.
Crowe, C. T., REVIEW—Numerical models for dilute gas-particle flows, *J. Fluids Eng.*, *104*, 297–303, 1982.
Denlinger, R. P., A model for generation of ash clouds by pyroclastic flows, with application to the 1980 eruption to Mt. St. Helens, Washington, *J. Geophys. Res.*, *92*, 10,284–10,298, 1987.
Dobran, F., Constitutive equations for multiphase mixtures of fluids, *Int. J. Multiphase Flow*, *10*, 273–305, 1984.
Dobran, F., Theory of multiphase mixtures, *Int. J. Multiphase Flow*, *11*, 1–30, 1985.
Dobran, F., Liquid and gas-phase distributions in a jet with phase change, *J. Heat Transfer*, *110*, 955–960, 1988.
Dobran, F., *Theory of Structured Multiphase Mixtures*, Springer-Verlag, New York, 1991.
Dobran, F., Nonequilibrium flow in volcanic conduits and application to the eruptions of Mt. St. Helens on May 18, 1980, and Vesuvius in AD 79, *J. Volcanol. Geotherm. Res.*, *49*, 285–311, 1992.
Dobran, F., and F. Mulargia, Prospects for the simulation of volcanic eruptions, *Rep. VSG91-1*, Giardini, Pisa, Italy, 1991.
Dobran, F., F. Barberi, and C. Casarosa, Modeling of volcanological processes and simulation of volcanic eruptions, *Rep. VSG90-1*, Giardini, Pisa, Italy, 1990.
Eldighidy, S. M., R. Y. Chen, and R. A. Comparin, Deposition of suspensions in the entrance of a channel, *J. Fluid Eng.*, *99*, 365–370, 1977.
Fan, Z. Q., B. Zhang, and J. Ding, Prediction of gas-particle two-phase flow in combustion, in *Proceedings of Institute Symposium Workshop on Particulate and Multiphase Processes*, edited by T. N. Veziroglu, pp. 287–306, Hemisphere, Washington, D. C., 1985.
Harlow, F. H., and A. A. Amsden, Numerical calculation of multiphase fluid flow, *J. Comput. Phys.*, *17*, 19–52, 1975.
Hoblitt, R. P., Observations of the eruptions of July 22 and August 7, 1980, at Mt. St. Helens, Washington, *U.S. Geol. Surv. Prof. Pap.*, *1335*, 1986.
Ishii, M., *Thermo-Fluid Dynamic Theory of Two-Phase Flows*, Eyrolles, Paris, 1975.
Jenkins, J. T., and S. B. Savage, A theory for the rapid flow of identical, smooth, nearly elastic, spherical particles, *J. Fluid Mech.*, *130*, 187–202, 1983.
Kieffer, S. W., Factors governing the structure of volcanic jets, in *Explosive Volcanism: Inception, Evolution, and Hazards*, pp. 143–157, National Academy Press, Washington, D. C., 1984.
Kieffer, S. W., and B. Sturtevant, Laboratory studies of volcanic jets, *J. Geophys. Res.*, *89*, 8253–8268, 1984.
Liepmann, H. W., and A. Roshko, *Elements of Gasdynamics*, John Wiley, New York, 1957.
Lun, C. K. K., S. B. Savage, D. J. Jeffrey, and N. Chepurnity, Kinetic theories for granular flow: Inelastic particles in Couette flow and slightly inelastic particles in a general flow field, *J. Fluid Mech.*, *140*, 223–256, 1984.
Ogawa, S., A. Umemura, and N. Oshima, On the equations of fully fluidized granular materials, *Z. Angew. Math. Phys.*, *31*, 483–493, 1980.
Rampino, M. R., and S. Self, Historic eruptions of Tambora (1815), Krakatau (1883), Agung (1963); their stratospheric aerosols and climatic impact, *Quat. Res.*, *18*, 127–143, 1982.
Rampino, M. R., and S. Self, Volcanic winter and accelerated glaciation following the Taba super-eruption, *Nature*, *359*, 50–52, 1992.
Rose, W. I., and C. A. Chesner, Dispersal of ash in the great Toba eruption, 75 ka, *Geology*, *15*, 913–917, 1987.
Savage, S. B., Streaming motions in a bed of vibrationally fluidized dry granular material, *J. Fluid Mech.*, *194*, 457–478, 1988.
Self, S., and M. R. Rampino, The 1883 eruption of Krakatau, *Nature*, *294*, 699–704, 1981.
Self, S., R. S. J. Sparks, B. Booth, and G. P. L. Walker, The 1973 Heimey strombolian scoria deposit, Iceland, *Geol. Mag.*, *111*, 539–548, 1974.
Sigurdsson, H., and S. Carey, Plinian and co-ignimbrite tephra fall from the 1815 eruption of Tambora volcano, *Bull Volcanol.*, *51*, 243–270, 1989.
Smith, R. L., Ash flows, *Geol. Soc. Am. Bull.*, *71*, 795–842, 1960.
Sparks, R. S. J., and T. C. Huang, The volcanological significance of deep-sea ash layers associated with ignimbrites, *Geol. Mag.*, *117*, 425–436, 1980.
Sparks, R. S. J., and L. Wilson, A model for the formation of ignimbrite by gravitational column collapse, *J. Geol. Soc. London*, *132*, 441–451, 1976.
Sparks, R. S. J., L. Wilson, and G. Hulme, Theoretical modeling of the generation, movement, and emplacement of pyroclastic flows by column collapse, *J. Geophys. Res.*, *83*, 1727–1739, 1978.
Valentine, G. A., and K. H. Wohletz, Numerical models of plinian eruption columns and pyroclastic flows, *J. Geophys. Res.*, *94*, 1867–1887, 1989*a*.
Valentine, G. A., and K. H. Wohletz, Environmental hazards of pyroclastic flows determined by numerical models, *Geology*, *17*, 641–644, 1989*b*.
Valentine, G. A., K. H. Wohletz, and S. W. Kieffer, Sources of unsteady column dynamics in pyroclastic flow eruptions, *J. Geophys. Res.*, *96*, 21,887–21,892, 1991.
Valentine, G. A., K. H. Wohletz, and S. W. Kieffer, Effects of topography of facies and compositional zonation in caldera-related ignimbrites, *Geol. Soc. Am. Bull.*, *104*, 154–165, 1992.
Wakao, N., S. Kaguei, and T. Funazkri, Effect of fluid dispersion coefficients on particle-to-fluid heat transfer coefficients in packed beds, *Chem. Eng. Sci.*, *34*, 325–336, 1979.
Walker, G. P. L., Explosive volcanic eruptions—A new classification theme, *Geol. Rundsch.*, *62*, 431–446, 1973.
Walker, G. P. L., Generation and dispersal of fine ash and dust by volcanic eruptions, *J. Volcanol. Geotherm. Res.*, *11*, 81–92, 1981.
Walker, G. P. L., Origin of coarse lithic breccias near ignimbrite source vents, *J. Volcanol. Geotherm. Res.*, *25*, 157–171, 1985.
Wallis, G. B., *One-Dimensional Two-Phase Flow*, McGraw-Hill, New York, 1969.
Wilson, C. J. N., The Taupo eruption, New Zealand II. The Taupo ignimbrite, *Philos. Trans. R. Soc. London, Ser. A*, *314*, 229–310, 1985.
Wilson, C. J. N., and G. P. L. Walker, Ignimbrite depositional facies: The anatomy of a pyroclastic flow, *J. Geol. Soc. London*, *139*, 581–592, 1982.
Wilson, L., Explosive volcanic eruptions, III, Plinian eruption columns, *Geophys. J. R. Astron. Soc.*, *45*, 543–556, 1976.
Wilson, L., and G. P. L. Walker, Explosive volcanic eruptions, VI, Ejecta dispersal in plinian eruptions: The control of eruption conditions and atmospheric properties, *Geophys. J. R. Astron. Soc.*, *89*, 657–679, 1987.
Wohletz, K. H., and G. A. Valentine, Computer simulations of explosive volcanic eruptions, in *Magma Transport and Storage*, edited by M. P. Ryan, pp. 113–135, John Wiley, New York, 1990.
Wohletz, K. H., and G. A. Valentine, Supercomputer simulations of explosive volcanism, in Prospects for the Simulation of Volcanic Eruptions, edited by F. Dobran and F. Mulargia, *Rep. VSG91-1*, pp. 53–56, Giardini, Pisa, Italy, 1991.
Wohletz, K. H., T. R. McGetchin, M. T. Sandford II, and E. M. Jones, Hydrodynamic aspects of caldera-forming eruptions: Numerical models, *J. Geophys. Res.*, *89*, 8269–8285, 1984.
Woods, A. W., A fluid dynamics and thermodynamics of eruption columns, *Bull. Volcanol.*, *50*, 169–193, 1988.
Woods, A. W., and K. Wohletz, Dimensions and dynamics of co-ignimbrite eruption columns, *Nature*, *350*, 225–227, 1991.
Wright, J. V., A. L. Smith, and S. Self, A working terminology of pyroclastic deposits, *J. Volcanol. Geotherm. Res.*, *8*, 315–336, 1980.

F. Dobran and A. Neri, GNV, Università di Pisa, Via S. Maria 53, 56100 Pisa, Italy.

G. Macedonio, CNR, Centro di Studio per la Geologia Strutturale e Dinamica dell'Appennino, Via S. Maria 53, 56100 Pisa, Italy.

(Received March 13, 1992;
revised August 19, 1992;
accepted October 7, 1992.)